`

Synthesis of FeNi based ZIF derived Electrocatalyst for Oxygen Reduction Reaction

By

Muhammad Umair

Reg. No. 00000318741

Session 2019-21

Supervised by

Dr. Naseem Iqbal

US-Pakistan Center for Advanced Studies in Energy (USPCAS-E)

National University of Sciences and Technology (NUST)

Islamabad, Pakistan

June 2022

`

Synthesis of FeNi based ZIF derived Electrocatalyst for Oxygen Reduction Reaction

By

Muhammad Umair

Reg. No. 00000318741

Session 2019-21

Supervised by

Dr. Naseem Iqbal

A Thesis Submitted to the US-Pakistan Center for Advanced Studies in Energy in partial fulfillment of the requirements for the degree of

MASTER of SCIENCE in

Energy Systems Engineering

US-Pakistan Center for Advanced Studies in Energy (USPCAS-E) National University of Science and Technology (NUST)

Islamabad, Pakistan

June 2022

`

THESIS ACCEPTANCE CERTIFICATE

Certified that final copy of MS/MPhil thesis written by **Muhammad Umair Imtiaz** (Registration No. 00000318741), of US-Pakistan Center for Advanced Studies in Energy (USPCAS-E) has been vetted by undersigned, found complete in all respects as per NUST Statues/Regulations, is within the similarity indices limit and is accepted as partial fulfillment for the award of MS degree. It is further certified that necessary amendments as pointed out by GEC members of the scholar have also been incorporated in the said thesis.

Signature: _____

Name of Supervisor: _____

Date: _____

Signature (HOD): _____

Date: _____

Signature (Dean/Principal): _____

Date: _____

`

Certificate

This is to certify that work in this thesis has been carried out by **Muhammad Umair Imtiaz** and completed under my supervision in Synthesis and Energy Storage laboratory, US-Pakistan Center for Advanced Studies in Energy (USPCAS-E), National University of Sciences and Technology, H-12, Islamabad, Pakistan.

Supervisor: _____

Prof. Dr. Naseem Iqbal
USPCAS-E
NUST, Islamabad

GEC member 1: _____

Dr. Ghulam Ali
USPCAS-E
NUST, Islamabad

GEC member 2: _____

Dr. Mustafa Anwar
USPCAS-E
NUST, Islamabad

GEC member 3: _____

Dr. Nadia Shahzad
USPCAS-E
NUST, Islamabad

HOD-ESE: _____

Dr. Rabia Liaquat
USPCAS-E
NUST, Islamabad

Dean/Principal: _____

Prof. Dr. Adeel Waqas
USPCAS-E
NUST, Islamabad

`

Dedication

To my parents, who supported me in every aspect of life and my siblings.

`

Abstract

Oxygen reduction (ORR) and evolution reactions are involved in oxygen electrochemistry. It is critical for ORR to produce highly effective non-noble metal catalysts to enhance the slower reaction kinetics. Today's research is focused on highly efficient electrocatalysts for oxygen reduction reaction (ORR) in fuel cells with minimal or negligible Pt use. A Zeolitic Imidazolate Framework (ZIF)-derived catalyst has been developed for fuel cell applications that can provide a hollow framework of nitrogen doped nanoporous carbon with excellent ORR activity. Here we report the synthesis of FeNi bimetallic electrocatalyst derived from zeolitic imidazole frameworks (ZIFs), FeNi nanoalloys embedded in N-doped carbon (FeNi-NC) containing carbon nanotubes and porous carbon exhibits superior performance for oxygen reduction reaction (ORR). The FeNi-NC showed remarkable performance in KOH with the onset and half wave potential of 0.99 V and 0.89 V vs RHE, respectively. This catalyst shows superior methanol tolerance against commercial platinum (Pt/C). The excellent activity and stability can be ascribed to the interaction between FeNi active sites and N-doped carbon, the unique nanostructure composed of porous carbon and carbon nanotubes with a high graphitization degree.

Keywords: Oxygen reduction reaction (ORR), Metal organic framework (MOF), Zeolite imidazole framework (ZIF), Commercial Platinum (Pt/C), Nano-porous carbon (NPC).

`

Table of Contents

`

`

`

`

List of Figures

`

`

`

List of Tables

`

List of publications

1 **Umair Imtiaz,** Naseem Iqbal, Tayyaba Noor, M Zain Bin Amjad, M. Arslan Raza, Asad Ali, Junkuo Gao, "ZIF-8 derived FeNi-NC Electrocatalyst for Oxygen Reduction Reaction" Journal: International Journal of Hydrogen Energy, 2022 (Under Review)

2 Asad Ali, Naseem Iqbal, Tayyaba Noor, **Umair Imtiaz,** "Nanostructured Mn-doped Zn-N-C @reduced graphene oxide as high performing electrocatalyst for oxygen reduction reaction" Journal: Journal of Electroanalytical Chemistry, 2022 (https://doi.org/10.1016/j.jelechem.2022.116324)

`

List of Abbreviations

AFC	Alkaline fuel cell
2mim	2-methyl imidazole
ZIF	Zeolite imidazole framework
MOF	Metal organic framework
NP	Nano porous carbon
BET	Brunauer Emmett Teller
N	Nitrogen
CA	Chronoamperometry
CB	Carbon Black
CE	Counter Electrode
CHP	Combined Heat and Power Efficiency
CNT’s	Carbon Nanotubes
CP	Controlled Potential
CV	Cyclic Voltammetry
DC	Direct Current
DI	Di-Ionized Water
DMFC	Direct Methanol Fuel Cell
DOE	Department of Energy
EDS	Energy Dispersive Spectroscopy
EIS	Electrochemical Impedance Spectroscopy
FC	Fuel cell
FTIR	Fourier Transform Infrared Spectroscopy
GCE	Glassy Carbon Electrode
ORR	Oxygen reduction reaction
HOR	Hydrogen Oxidation Reaction

`

CHAPTER 1 INTRODUCTION

1.1 Background

Energy is essential for meeting fundamental human requirements. It is necessary for human health, daily life, communication, and mobility, as well as economic and social progress and well-being in general. The world's energy demands have risen rapidly in recent years, and they are likely to rise considerably more as the world's population grows along with economic and technological advancements. The world's population is expected to reach 9 billion people by 2050 [1]. The US Energy Information Administration (EIA) forecasts a nearly 50% increase in global energy use between 2018 and 2050 [2].

Fossil fuels have been the primary source of energy since the industrial revolution and have risen in use to approximately 10,000 million tons of oil equivalent. Fossil fuels produced over 80% of all primary energy worldwide in 2010, and they are projected to continue to play a key role in meeting global energy needs in the future. By 2040, fossil fuels are expected to account for 78% of total global energy consumption [3].

Fossil fuels have long been recognized as having harmful effects on the environment. Their combustion and consumption release huge amounts of greenhouse gases into the atmosphere, contributing to climate change and global warming [4]. According to the EPA (United States Environmental Protection Agency), carbon dioxide (CO2) emissions from fossil fuel and industrial operations account for 65 percent of overall greenhouse gas (GHG) emissions [5].

In 1992, the United Nations Framework Convention on Climate Change (UNFCCC) laid the groundwork for reducing GHG emissions, emphasizing that such a decrease is necessary to avert catastrophic environmental repercussions. Furthermore, in 2015, the United Nations adopted the 17 Sustainable Development Goals, which encompass subjects such as clean energy, climate change, and GHG emissions, with an aim of integrating GHG emission reduction policies and initiatives [6].

Energy is regarded to be a vital aspect of sustainable development, so limiting the use of fossil fuels and transitioning to renewable sources is one of the most important reduction

`

initiatives. Furthermore, the scarcity of fossil fuels and their high cost make the transition to renewable energy sources even more critical in order to provide energy security and meet energy demand. Over the period 1990–2015, renewable energy accounted for 17.5% of total final energy consumption worldwide, and it is predicted to be the fastest-growing energy source in the future [7].

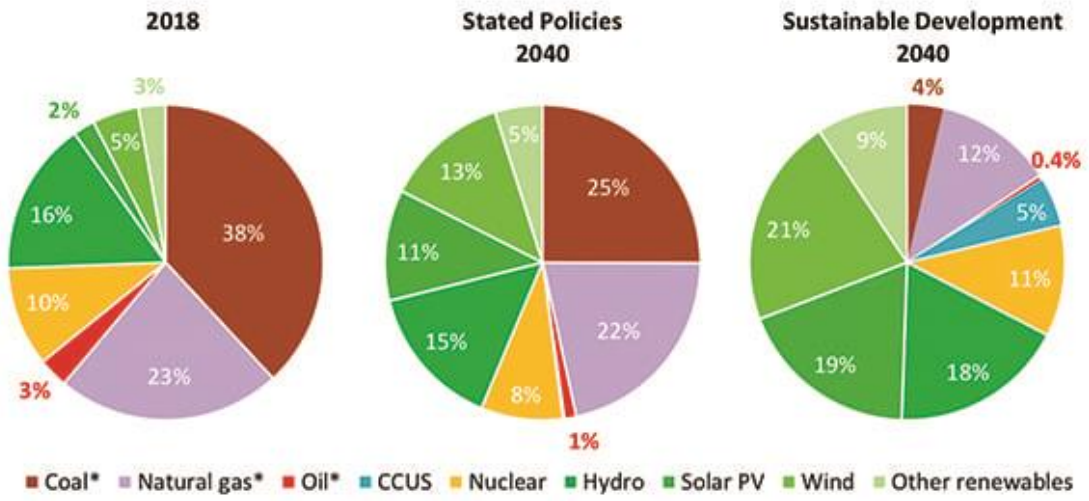

Figure 1.1 Total energy supplies in 2018. This figure was taken and used without any modification from reference [3]

1.2 Alternative Energy resources:

As a developing country, Pakistan faces enormous hurdles in meeting its energy demands with limited energy supplies. Fossil fuel is the primary source of energy for power generation, which has environmental consequences [8]. Renewable energy contributes only a small fraction of the overall energy supply of the country's energy supply situation, owing to a lack of investment and effort [9].

In view of these circumstances, it is necessary to develop and improve alternative energy sources that are both more reliable and environmentally beneficial. Increasing efforts have been committed to energy alternative sources, specifically wind energy, hydroelectric power, hydrogen energy, solar energy, and nuclear energy, that have already functioned as alternative energy sources to traditional fossil fuels. The use of environmentally

`

friendly hydrogen energy in hydrogen fuel cells is one of the most promising. Fuel cells are a viable alternative energy source with high energy output, as well as a clean and prospective future [10].

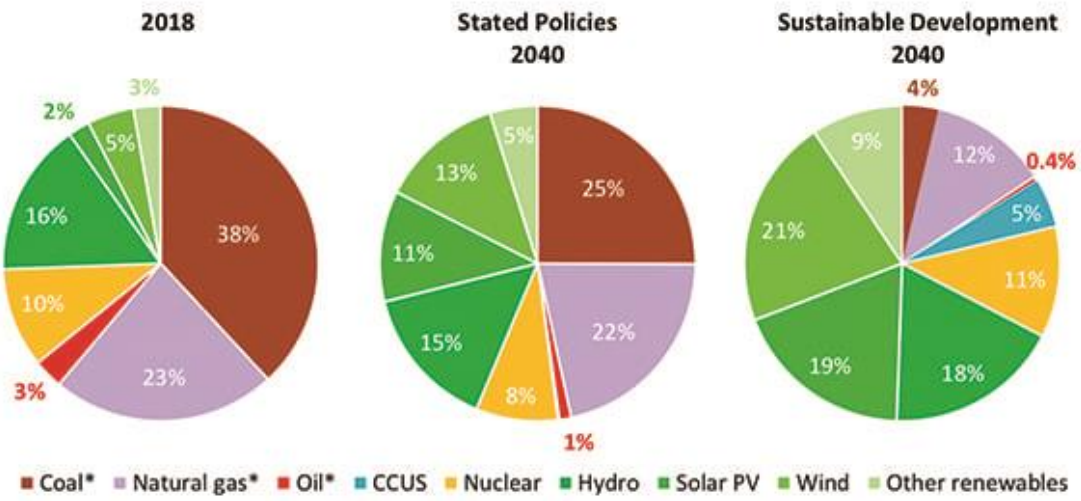

Figure 1.1 Total energy supplies in 2018. This figure was taken and used without any modification from reference [3]

1.3 Fuel cells

A fuel cell is an electrochemical cell that uses an electrochemical reaction to produce electrical energy from fuel. In order to sustain the processes that create electricity, these cells need a constant supply of fuel and an oxidizing agent (often oxygen). As a result, until the supply of fuel and oxygen is shut off, these cells can generate power indefinitely [11].

Sir William Robert Grove, a Welsh judge, inventor, and physicist, invented the first fuel cell in 1839. He created a fuel cell by mixing hydrogen and oxygen in the presence of an electrolyte, however the fuel cell's output is rather modest. This fundamental technology is still employed in fuel cells today. Fuel cells were first used commercially by NASA to power space capsules and satellites only a century after they were conceived in 1839. Many establishments, including industries, commercial buildings, and residential buildings, use these devices as their primary or secondary source of energy today [12].

`

When compared to other market technologies, fuel cells are thought to be more efficient. When it comes to portable, mobile, and stationary applications, photoelectric devices, solar thermal technologies, waste disposal technology, gas fired turbines, and nuclear power plants have substantially inferior energy efficiency than fuel cells. They do not release any hazardous waste, nor do they discharge any waste gases that contribute to global warming or other environmental issues. Fuel cells are preferred for portable applications because of their advantages in both gravimetric and volumetric energy densities. Because of their greater capacitive factors, they are also being used in the stationary industry [13].

Fuel cells are similar to batteries in that they both contain two electrodes and a working electrolyte sandwiched between the two electrodes. Internal oxidation-reduction reactions are involved in each of them. The discrepancy is due to the electrode composition, as well as the amount and kind of output current. Proton conducting medium electrodes are used in fuel cells, whereas metal electrodes are used in batteries. The main distinction between them is in terms of energy storage; batteries store energy and discharge current like a capacitor, whereas fuel cells operate as a continuous process, i.e., they take in fuel and continually produce current [14].

1.4 Types of fuel cells

Fuel cells are distinguished by the category of electrolyte employed. The sort of electrochemical reactions that take place in the cell, the catalysts which must be employed, the average temperature where the cell must operate, the material needed, as well as other characteristics are all determined by this categorization. These qualities influence the activities under which these cells seem to be particularly fit. Fuel cells exist in a range of sizes and shapes, with its own collection of advantages, disadvantages, and applications.

`

Table 1.1 Major types of fuels cells

Fuel Cell Type	Electrolyte	Operating Temperature	Electrical Efficiency	Applications	Advantages	Challenges
Polymer Electrolyte Membrane (PEM)	Perfluorosulfonic Acid	$<120^0$C	60%	Backup power Portable power Transportation	Low temperature Quick start-up	Expensive catalysts Sensitive to fuel impurities
Alkaline (AFC)	Aqueous Potassium Hydroxide	$<100^0$C	60%	Military Space Backup power	Wide range of stable materials allows lower cost components	Sensitive to CO_2 in fuel and air
Phosphoric Acid (PAFC)	Phosphoric Acid	150-200^{0}C	40%	Distributed generation	Suitable for CHP Increased tolerance to fuel impurities	Expensive catalysts Sulfur sensitive
Molten Carbonate (MCFC)	Molten Lithium, Sodium/Potassium Carbonates	600-700^{0}C	50%	Distributed generation	High Efficiency Fuel flexibility	Long start-up time Low power density
Solid Oxide (SOFC)	Yttria Stabilized Zirconia	500-1000^{0}C	60%	Auxiliary power Electric utility	High Efficiency Fuel flexibility Solid electrolyte	Break down of cell components

`

1.4.1 Alkaline Fuel cells

Alkaline fuel cells (AFCs) were among the first fuel cell technologies to also be developed, and they're the first to be extensively used throughout the US Space project to generate electrical energy and water on-board missions. In such fuel cells, the electrolyte is indeed a mixture of potassium hydroxide in water, and also the cathode and anode could be built of just a proportion of non metals. In past few years, unique AFCs with a polymer film as the electrolyte have been developed. Such fuel cells seem identical to standard PEM fuel cells, apart from that they were using as alkaline membrane rather than an acidic membrane. The explosive growth of electrochemical processes of the cell is essential for AFCs' high efficiency. They have indeed demonstrated savings of far more than 60% in aircraft applications [15].

The fact that such a fuel cell type is susceptible to carbon dioxide contamination is among the most serious issues it faces (CO_2). Because of carbonate formation, even a little concentration of CO_2 into the atmosphere will have a substantial effect on cell strength and reliability. Even though the circulatory mode introduces reverse current challenges, looping alkaline cells having aqueous electrolytes enable regular electrolyte replenishment, that assists reduce the effects of carbonate accumulation in the electrolyte. Absorption, accelerated degradation, and issues managing differential pressures are some challenges with liquid electrolyte devices. Alkaline membrane fuel cells (AMFCs) address these issues that they're less susceptible towards CO2 degradation then liquid-electrolyte AFCs. Nevertheless, CO2 tends to provide an influence on productivity, and AMFC efficiency and durability lag below PEMFCs. AMFCs are now being investigated for use in various applications between W to kW. AMFCs face issues in carbon dioxide sensitivity, membrane permeability and endurance, higher heat function, water management, power density, and anode electro catalysis [16].

The reactions taking place in AFCs are as follows:

At anode:

$$H_2 + 2OH^- \rightarrow 2H_2O + 2e^- \qquad \text{(eq. 1.1)}$$

At Cathode:

`

$$1/2O_2 + H_2O + 2e^- \rightarrow 2OH^- \qquad \text{(eq. 1.2)}$$

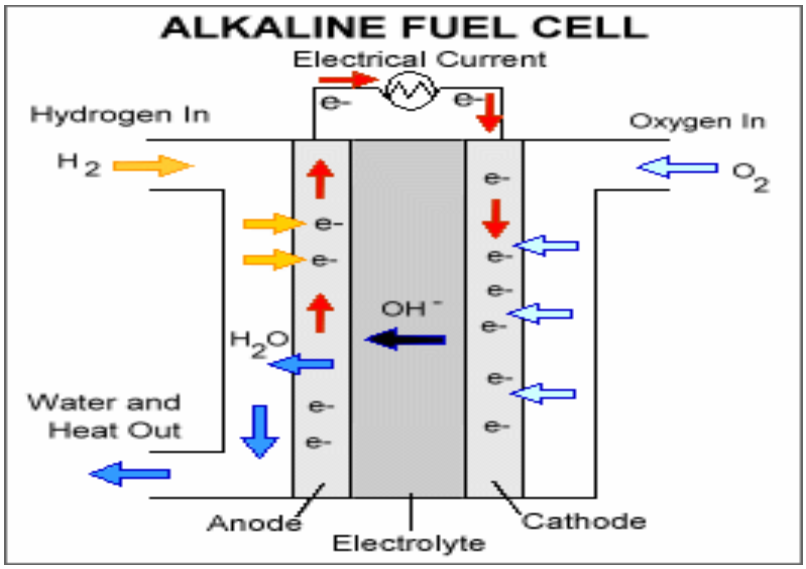

Figure 1.2 Alkaline fuel cell schematic diagram. This figure was taken and used without any modification from reference [15]

1.4.2 Phosphoric acid fuel cell

Fluid phosphoric acid serves as the electrolyte in phosphoric acid fuel cells (PAFCs). The acid is contained by a Teflon-bonded silicon carbide substrate with carbon based electrodes with a platinum catalyst. This diagram displays various electrochemical processes that take place in the cell.

The PAFC is classified as innovative fuel cell of "first generation." That is amongst the most developed cell types by being the first to further used widely. PAFCs were being used to operate big vehicles such as public buses, despite their primary usage in stationary power generation. PAFCs were generally susceptible to contaminants found in reformed fossil fuels unlike PEM cells that can rapidly "poisoned" by carbon monoxide, which attaches with a platinum catalyst at the anode, lowering the fuel cell's efficiency. PAFCs are far more than 85 percent functional if used for co-generation of heat and power, however they are less effective (37–42 percent) when it is used to produce electricity alone. PAFCs have a somewhat better efficiency than ignition power stations that are usually around 33% effective. PAFCs become less active than conventional fuel cells if the same weight and volume are used. As a consequence, such fuel cells were generally

`

large and hefty. PAFCs are therefore expensive. They demand far higher platinum catalyst loadings than other fuel cell types, therefore raises the cost [17].

The overall reactions are:

At anode:

$$H_2 \rightarrow 2H^+ + 2e^- \qquad \text{(eq. 1.3)}$$

At Cathode:

$$\tfrac{1}{2}O_2 + 2H^+ + 2e^- \rightarrow H_2O \qquad \text{(eq. 1.4)}$$

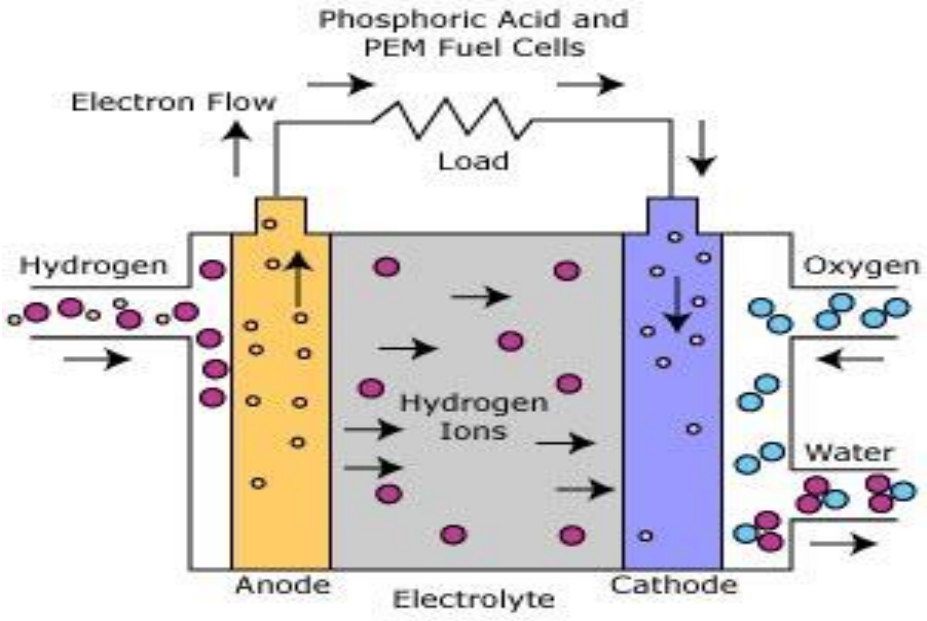

Figure 1.3 Schematic diagram of Phosphoric acid fuel cells. This figure was taken and used without any modification from reference [17]

1.4.3 Proton Exchange Membrane Fuel Cells

Proton exchange membrane (PEM) fuel cells provide a high power density while being light in weight and volume. PEM fuel cells are using a solid polymer electrolyte and porous carbon electrodes with either a platinum or platinum alloy catalyst. To operate, they only need hydrogen, oxygen out from air, and water. They are usually propelled by pure hydrogen supplied by reservoirs or reformers [18].

`

PEM fuel cells operate at a moderate temperature of 80°C (176°F). Moderate function allows them to operate quicker (lower warm-up delay) and places little strain upon components of the system, leading to increased durability. That does, unfortunately, involve the use of a noble-metal catalyst (often platinum) to split the electrons and protons of hydrogen, thus raises the system's price. Whereas if hydrogen is produced from a hydrocarbon fuel, an additional reactor is necessary to eliminate carbon monoxide from the fuel gas since the platinum catalyst is extremely sensitive to carbon monoxide poisoning. The price of this reactor goes up as well [19].

The majority of PEM fuel cells are used in transportation as well as several immobile applications. PEM fuel cells are ideal for use in vehicle applications such as autos, buses, and large trucks.

Following reactions take place in the PEMFC:

Hydrogen is electrochemically oxidized at the anode to produce protons and electrons. This is known as the hydrogen oxidation reaction (HOR):

$$H_2 \rightarrow 2H^+_{(aq)} + 2e^- \qquad E= 0V \qquad \text{(eq. 1.5)}$$

At Cathode side, the electrons are reacted with oxygen. The reactions is known as oxygen reduction reaction (ORR):

$$\frac{1}{2}O_2 + 2H^+ + 2e^- \rightarrow H_2O \qquad E°= 1.23V \qquad \text{(eq. 1.6)}$$

The overall reaction results in water and heat as by-product:

`

$$H_2 + \frac{1}{2}O_2 \rightarrow H_2O \qquad E°_{cell} = 1.23V \qquad \text{(eq. 1.7)}$$

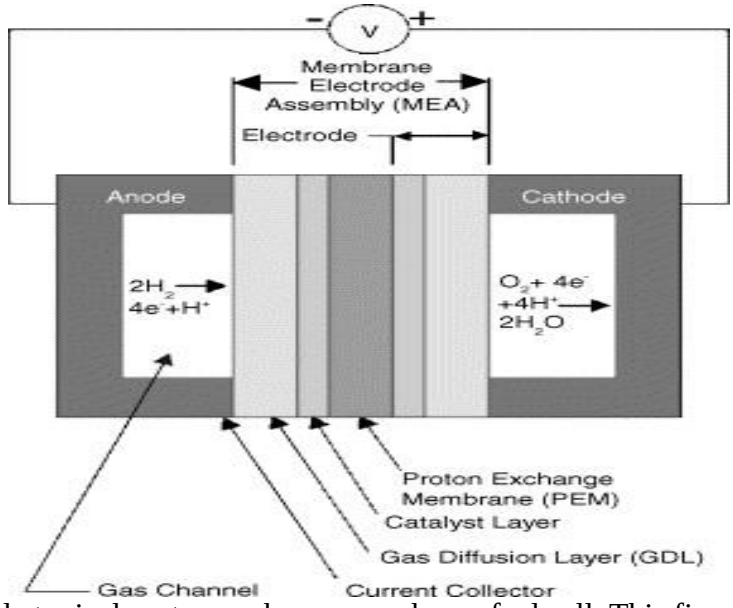

Figure 1.4 Single typical proton exchange membrane fuel cell. This figure was taken and used without any modification from reference [18]

1.4.4 Molten Carbonate fuel cell

Molten carbonate fuel cells (MCFCs) are now being investigated towards commercial, industrial, and military applications, including for coal and gas and fossil power plants. MCFCs were high-temperature fuel cells that have an electrolyte composed on molten carbonate salts floating inside a highly permeable, chemically stable ceramic lithium aluminium oxide substrate. Because they act at high temperatures of 650°C (about 1,200°F), non-precious metals could be used as catalysts at both the cathode and anode. This reduces costs. Increased efficiency is yet another factor MCFCs provide significant cost savings versus phosphoric acid fuel cells. Molten carbonate fuel cells, once paired with a rotor, might attain performances around 65 percent that is much higher than the 37–42 percent accuracy of a phosphoric acid fuel cell system. When excess heat is captured and used, average fuel efficiency can surpass 85 percent [20].

Unlike alkaline, phosphoric acid, and PEM fuel cells, MCFCs don't really require an additional converter to transform fuels such as natural gas and biogas to hydrogen. At the extreme temps employed in MCFCs, methane and other light hydrocarbons in all of these fuels were turned into hydrogen inside the fuel cell itself through a procedure known

`

internal reforming, that reduces costs. The primary disadvantage of current MCFC technology has been its limited lifetime. These cells' increased temperature, combined with the corrosive electrolyte they use, increase material degradation and rusting, leading to reduced cell life. Researchers already are looking on corrosion-resistant substances for elements and also fuel cell configurations that can double the present 40,000-hour (five-year) cell life without loss of performance [21].

In MCFC, following reactions takes place:

At anode:

$$H_2 + CO_3^{2-} \rightarrow H_2O + CO_2 + 2e^- \qquad \text{(eq. 1.8)}$$

At Cathode:

$$\frac{1}{2}O_2 + CO_2 + 2e^- \rightarrow CO_3^{2-} \qquad \text{(eq. 1.9)}$$

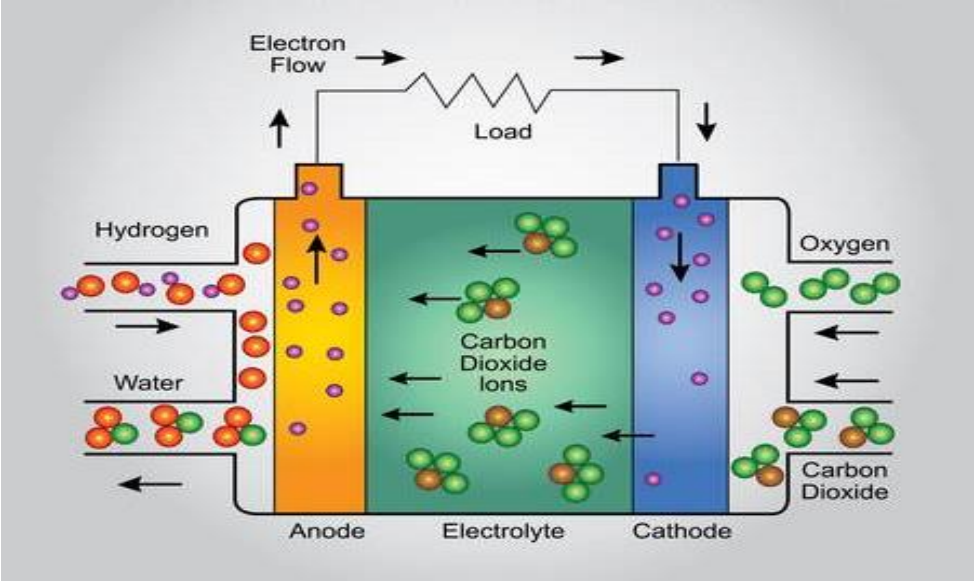

Figure 1.5 Schematic diagram of molten carbonate fuel cell. This figure was taken and used without any modification from reference [20]

1.4.5 Solid oxide fuel cell

In solid oxide fuel cells, the electrolyte is indeed a solid, non-porous ceramic substance (SOFCs). SOFCs have a conversion efficiency of around 60% when transforming fuel to electricity. For technologies that catch and utilize the system's extra heat, average fuel usage performance could approach 85 percent (cogeneration). SOFCs could resist

`

temperatures of up to 1,000 degrees Celsius (1,830 degrees Fahrenheit). In high-temperature processes, the need for a precious-metal catalyst is avoided, saving expenses. It also enables SOFCs to internally reform fuels, enabling it to employ a broader spectrum of fuels while minimizing the cost of integrating a reformer to such systems [22].

SOFCs are also the most sulfur-resistant fuel cells, with the ability to withstand orders of magnitude more Sulphur than other cell types. They are also unaffected by carbon monoxide, which can even be used as a fuel. This characteristic enables SOFCs to use natural gas, biogas, and coal-derived gases. There are drawbacks to high-temperature operation. It requires significant shielding to conserve heat and safeguard staff, which is great in energy reasons but unsuitable for transporting. Because of the high operating temperatures, material endurance is indeed an issue. The development of low-cost materials with excellent durability during cell operation conditions is the primary technical challenge for this technology. Researchers are working hard to develop reduced SOFCs that run at less than 700°C, have less endurance difficulties, are much less expensive. Lower-temperature SOFCs, but in the other hand, have been unable to outperform higher-temperature devices, and stacked materials for such a temperature range are actively being explored [23].

The overall reactions taking place in the cell are:

At anode:

$$H_2 + O^{2-} \rightarrow H_2O + 2e^- \qquad \text{(eq. 1.10)}$$

`

At cathode:

$$\frac{1}{2}O_2 + 2e^- \rightarrow O^{2-} \qquad \text{(eq. 1.11)}$$

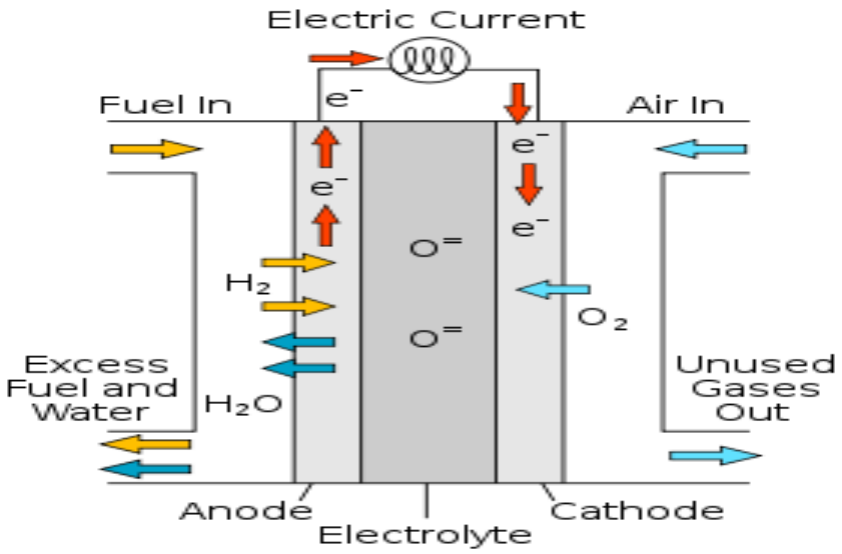

Figure 1.6 Schematic diagram of Solid oxide fuel cell. This figure was taken and used without any modification from reference [22]

1.5 Scope of research topic

Hydrogen-powered fuel cells are the greatest and most suitable substitutes for fossil fuels since they are significantly cleaner and provide more energy than traditional fuels. The proton exchange membrane fuel cell (PEMFC) is the most viable candidate among various types of fuel cells for both stationary and mobile applications, giving higher power density at lower operating temperatures than other fuel cells. The system still faces numerous hurdles, such as slow oxygen reduction reaction kinetics, a costly Pt catalyst, catalyst degradation and fuel storage. Many studies are underway with a significant focus on developing a high-performance non-platinum metal electrocatalyst (NPME) to replace the Pt-based catalyst, which is one of the critical points in the increase of fuel cell operating costs. For electrochemical energy storage and conversion systems, the oxygen reduction process (ORR) is the most significant and most vital. For a long time, noble metals, such as platinum (Pt), have been employed to solve this problem. However, their rarity, poor stability, and limited methanol tolerance have compelled researchers to discover and

`

create materials that are more robust, have higher activity, electrochemical stability, and corrosion tolerance, and are less expensive for their use in ORR.

Metal-organic frameworks (MOFs) have opened up a new world of adjustable porous crystalline materials that can be used as a template or precursor in fuel cells, batteries, gas storage, sensors, supercapacitors, and catalysis. As precursors for the production of porous, nitrogen-rich nanocarbon frameworks, zeolitic imidazolate frameworks (ZIFs) have been found to have good catalytic performance. For the production of ZIF-derived M-N-C (metal-nitrogen-carbon) catalyst, several metal precursors such as Ni, Co, Fe, Zn, Cu, and Mn were employed. This catalyst is claimed to be an ideal candidate with strong ORR kinetics. In alkaline media, the Fe-doped ZIF-8 catalyst outperformed others in terms of ORR. Similarly, ZIF-derived N-doped carbon fibres have shown high ORR catalytic activity. Based on these benefits, novel bimetallic nitrogen-doped carbon electrocatalysts generated from ZIF are expected to be employed in fuel cell applications in the future.

1.6 Research Objectives

This research has following main objectives:

1. To synthesize FeNi-ZIF derived electro-catalysts and study their activity for oxygen reduction reaction (ORR).
2. To study the internal structure of FeNi-ZIF derived electro-catalyst through different characterization techniques.
3. To carry out electrochemical measurements to evaluate the performance of these electro-catalysts.

`

Summary

This chapter gives an overview of the worldwide energy landscape as well as the Pakistani energy situation. This chapter covers a variety of alternative energy sources, as well as fuel cells and their various kinds.

`

References

[1] J. J. Klemeš, P. S. Varbanov, P. Ocłoń, and H. H. Chin, "Towards Efficient and Clean Process Integration: Utilisation of Renewable Resources and Energy-Saving Technologies," *Energies* , vol. 12, no. 21. 2019, doi: 10.3390/en12214092.

[2] M. Höök and X. Tang, "Depletion of fossil fuels and anthropogenic climate change—A review," *Energy Policy*, vol. 52, pp. 797–809, 2013, doi: https://doi.org/10.1016/j.enpol.2012.10.046.

[3] S. Suman, "Hybrid nuclear-renewable energy systems: A review," *J. Clean. Prod.*, vol. 181, pp. 166–177, 2018, doi: https://doi.org/10.1016/j.jclepro.2018.01.262.

[4] L. Chiari and A. Zecca, "Constraints of fossil fuels depletion on global warming projections," *Energy Policy*, vol. 39, no. 9, pp. 5026–5034, 2011, doi: https://doi.org/10.1016/j.enpol.2011.06.011.

[5] I. Dincer, "Renewable energy and sustainable development: a crucial review," *Renew. Sustain. Energy Rev.*, vol. 4, no. 2, pp. 157–175, 2000, doi: https://doi.org/10.1016/S1364-0321(99)00011-8.

[6] O. Ellabban, H. Abu-Rub, and F. Blaabjerg, "Renewable energy resources: Current status, future prospects and their enabling technology," *Renew. Sustain. Energy Rev.*, vol. 39, pp. 748–764, 2014, doi: https://doi.org/10.1016/j.rser.2014.07.113.

[7] K. Srirangan, L. Akawi, M. Moo-Young, and C. P. Chou, "Towards sustainable production of clean energy carriers from biomass resources," *Appl. Energy*, vol. 100, pp. 172–186, 2012, doi: https://doi.org/10.1016/j.apenergy.2012.05.012.

[8] N. L. Panwar, S. C. Kaushik, and S. Kothari, "Role of renewable energy sources in environmental protection: A review," *Renew. Sustain. Energy Rev.*, vol. 15, no. 3, pp. 1513–1524, 2011, doi: https://doi.org/10.1016/j.rser.2010.11.037.

[9] N. Ç. E.-M. P. E.-H. L. O. Junior, "Cellulose Grafting by Atom Transfer Radical Polymerization Method," Rijeka: IntechOpen, 2015, p. Ch. 3.

[10] S. G. Yalew *et al.*, "Impacts of climate change on energy systems in global and

`

regional scenarios," *Nat. Energy*, vol. 5, no. 10, pp. 794–802, 2020, doi: 10.1038/s41560-020-0664-z.

[11] K. Saikia, B. K. Kakati, B. Boro, and A. Verma, "Current Advances and Applications of Fuel Cell Technologies BT - Recent Advancements in Biofuels and Bioenergy Utilization," P. K. Sarangi, S. Nanda, and P. Mohanty, Eds. Singapore: Springer Singapore, 2018, pp. 303–337.

[12] G. J. K. Acres, "Recent advances in fuel cell technology and its applications," *J. Power Sources*, vol. 100, no. 1, pp. 60–66, 2001, doi: https://doi.org/10.1016/S0378-7753(01)00883-7.

[13] "The Long History of Fuel Cells," *Fuel Cells*. pp. 25–40, Mar. 09, 2012, doi: https://doi.org/10.1002/9781118191323.ch2.

[14] P. Agnolucci, "Economics and market prospects of portable fuel cells," *Int. J. Hydrogen Energy*, vol. 32, no. 17, pp. 4319–4328, 2007, doi: https://doi.org/10.1016/j.ijhydene.2007.03.042.

[15] M. A. Al-Saleh, S. Gultekin, A. S. Al-Zakri, and A. A. A. Khan, "Steady state performance of copper impregnated Ni/PTFE gas diffusion electrode in alkaline fuel cell," *Int. J. Hydrogen Energy*, vol. 21, no. 8, pp. 657–661, 1996, doi: https://doi.org/10.1016/0360-3199(95)00122-0.

[16] S. AHN and B. J. TATARCHUK, "Fibrous metal–carbon composite structures as gas diffusion electrodes for use in alkaline electrolyte," *J. Appl. Electrochem.*, vol. 27, no. 1, pp. 9–17, 1997, doi: 10.1023/A:1026454513293.

[17] Y. Ansari, T. G. Tucker, and C. A. Angell, "A novel, easily synthesized, anhydrous derivative of phosphoric acid for use in electrolyte with phosphoric acid-based fuel cells," *J. Power Sources*, vol. 237, pp. 47–51, 2013, doi: https://doi.org/10.1016/j.jpowsour.2013.03.003.

[18] N. F. Asri, T. Husaini, A. B. Sulong, E. H. Majlan, and W. R. W. Daud, "Coating of stainless steel and titanium bipolar plates for anticorrosion in PEMFC: A review," *Int. J. Hydrogen Energy*, vol. 42, no. 14, pp. 9135–9148, 2017, doi:

`

https://doi.org/10.1016/j.ijhydene.2016.06.241.

[19] S. Karimi, N. Fraser, B. Roberts, and F. R. Foulkes, “A Review of Metallic Bipolar Plates for Proton Exchange Membrane Fuel Cells: Materials and Fabrication Methods,” *Adv. Mater. Sci. Eng.*, vol. 2012, p. 828070, 2012, doi: 10.1155/2012/828070.

[20] V. V Belousov, “Next-Generation Electrochemical Energy Materials for Intermediate Temperature Molten Oxide Fuel Cells and Ion Transport Molten Oxide Membranes,” *Acc. Chem. Res.*, vol. 50, no. 2, pp. 273–280, Feb. 2017, doi: 10.1021/acs.accounts.6b00473.

[21] V. V Belousov and S. V Fedorov, “Bubble nucleation in core–shell structured molten oxide-based membranes with combined diffusion-bubbling oxygen mass transfer: experiment and theory,” *Phys. Chem. Chem. Phys.*, vol. 23, no. 41, pp. 24029–24038, 2021, doi: 10.1039/D1CP03355G.

[22] Y. Akdeniz, B. Timurkutluk, and C. Timurkutluk, “Development of anodes for direct oxidation of methane fuel in solid oxide fuel cells,” *Int. J. Hydrogen Energy*, vol. 41, no. 23, pp. 10021–10029, 2016, doi: https://doi.org/10.1016/j.ijhydene.2016.03.169.

[23] M. Ahn, J. Lee, and W. Lee, “Nanofiber-based composite cathodes for intermediate temperature solid oxide fuel cells,” *J. Power Sources*, vol. 353, pp. 176–182, 2017,

`

CHAPTER 2 LITERATURE REVIEW

2.1 Oxygen reduction reaction

The oxygen reduction reaction (ORR) has been the subject of extensive investigation throughout the last century [1]. This is because ORR is crucial for energy conversion, particularly in fuel cells and metal-air batteries [2]. ORR is the most important cathodic process in polymer electrolyte membrane fuel cells. Pt remains the most effective ORR catalyst among all materials studied [3]. The fundamental issue with Pt is that it belongs to the periodic table's platinum group, that are precious metals and therefore too expensive for the development of fuel cells. As a result, additional research has been conducted in an attempt to generate alternative electrocatalysts that can be utilized [4].

Oxygen reduction in aqueous media occurs predominantly through different routes: a four-electron reduction mechanism from O_2 to H_2O or a two-electron reduction route from O_2 to H_2O_2. Damjanovic et al. proposed the most generally recognized pathway of ORR, which Wroblowa et al. further modified [5], making the sophisticated oxygen reaction mechanism upon that surface of the metal easier to understand [6]. They suggest that ORR proceeds at comparable rates along two concurrent reaction routes. In PEMFCs, a four-electron exchange is desired [7].

When seen in aqueous acidic media, the ORR can occur in two ways:

The overall reaction from O_2 to H_2O (4-electrons reduction):

$$O_2 + 4H^+ + 4e^- \rightarrow 2H_2O \qquad E = 1.29\ V \qquad \text{(eq. 2.1)}$$

2 steps conversion of O_2 to H_2O (2-electron reduction):

$$O_2 + 2H^+ + 2e^- \rightarrow H_2O_2 \qquad E = 0.70\ V \qquad \text{(eq. 2.2)}$$

`

$H_2O_2 + 2H^+ + 2e^- \rightarrow 2H_2O$ E = 1.76 V (eq. 2.3)

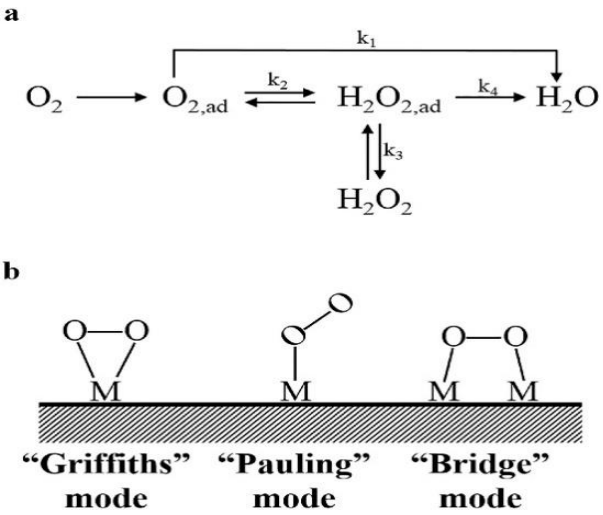

Figure 2.1 (a) Reaction pathways of ORR in acidic media. (b) Modes of O_2 adsorption on catalyst surface. This figure was taken and used without any modification from reference [9].

The O_2 adsorption mostly on catalyst surface activates the ORR, which regulates the electron process. The three adsorption mechanisms are considered on the catalyst [5]. The Griffiths model (one site), the Bridge model (two sites), and the Pauling model (one site) are suggested for 4-electron reactions, while the Pauling model (one site) is recommended for 2-electron reactions (Figure 2.1b). Because peroxide buildup in the electrolyte of fuel cells is unfavorable, 4-electron reduction is preferred. Regardless, it involves a number of mechanisms in which oxygen gas is split at the surface and reassembles with H_2 to form H_2O. As a consequence, the process has slow kinetics and necessitates the use of an efficient catalyst [9].

2.2 ZIF derived M-N-C Electrocatalysts for ORR

The most difficult part of creating functionalized ORR/OER electrocatalysts is locating effective materials with excellent intrinsic activity. Precious metals and their oxides have been recognised as unifunctional catalysts [10]. In the previous decade, bifunctional electrocatalysts derived from ZIF and transition-metal-based materials are intensively researched [7].

`

2.2.1 Noble Metals-Based M–N–C Electrocatalysts

Aside from transition metals, creating atomically distributed precious metals-based M–N–C electrocatalysts can drastically reduce the cost of ORR catalysts. For years, researchers have been interested in atomic Pt–N–C electrocatalysts because they are located at the top of the volcano map. Furthermore, palladium has greater ORR activity. Recent research have demonstrated that Pd-doped ZIF-8 was an excellent technique to produce Pd–N–C catalyst to minimise costs without compromising good catalytic performance to take benefit of Pd's high activity. The effective catalytic active sites were considerably increased because the Pd–Nx sites were mostly positioned on the carbon surface. As a result, Pd–N–C electrocatalysts with E_{onset} = 1.000 V (Eonset: onset potential) and $E_{1/2}$ = 0.898 V singled out as the superior ORR electrocatalysts [8]. However, the carbon-supported Pt–N_4 or Pd–N_4 catalytic sites were active for ORR only in alkaline circumstances and were less efficient in acidic settings. Using a progressive coordinated technique, the researchers recently added Ir to ZIF to generate an Ir–N–C structure. The weight of Ir was 4.5 wt. percent, presenting a novel approach for atomically dispersing rare metals in extremely high loading proportions. The E_{onset} value of 0.923 V and $E_{1/2}$ value of 0.831 V vs RHE in acidic media for the produced Ir–N–C were equivalent to the performance of commercialized Pt/C (E_{onset}: 0.952 V; $E_{1/2}$: 0.862 V) [9].

2.2.2 Bimetallic ZIF derived M–N–C Electrocatalysts

Some researchers have reported creating atom-pair-based M–N–C electrocatalysts based on the synergetic effects of two distinct metal atoms (e.g., Fe–Co–N–C, Fe–Cu–N–C) to overcome the activity/stability limitations of M–N–C [10]. As shown in Figure 2.2a, the Fe–Co bimetallic sites-based ORR catalysts including double isolated atoms attaching on ZIF-derived carbon nanoparticles (Fe–Co–N–C) were prepared using an adsorption–calcination approach. The dodecahedral geometry of Fe–Co–N–C was revealed by the results (Figure 2.2b), and the interface turned rougher and porous following pyrolysis. Fe and Co were grouped together towards the matrix surface, although their dispersion was not uniform. The Fe and Co concentrations were discovered to be 0.964 wt% and 0.218 wt%, respectively. Moreover, across all sorts of catalysts, the Fe–Co–N–C displayed the

`

best ORR catalytic properties, with an extraordinary $E_{1/2}$ of 0.920 V (Figure 2.2c), implying a huge opportunity for constructing long-lasting energy conversion devices employing such fully prepared Fe–Co–C–N electrocatalysts [11].

Cu has high ORR activity amongst some of the non-noble transition metals, according to theoretical simulations [12]. However, due to the high diffusion rate of Cu ions, Cu-based carbon materials generated during pyrolysis process always exhibit poor electrocatalytic activity. To solve this problem, researchers employed Cu sheet to react with Fe^{3+} and ZIF, with the Fe^{3+} stripping the Cu to introduce Fe^{2+} and Cu^{2+}, resulting in the atomic Fe^{2+} and Cu^{2+} co-doped precursors; subsequently carbonization was used to produce the Cu and Fe biatomic catalyst, Cu–Fe–N–C. (Figure 2.2f). Because of its bimetallic active sites and high nitrogen doping level, the Cu–Fe–N–C demonstrated better ORR performance than the bare Fe–N–C, opening up a new avenue for designing atom-pair-based M–N–C electrocatalysts using a broader toolset of transition metals [13].

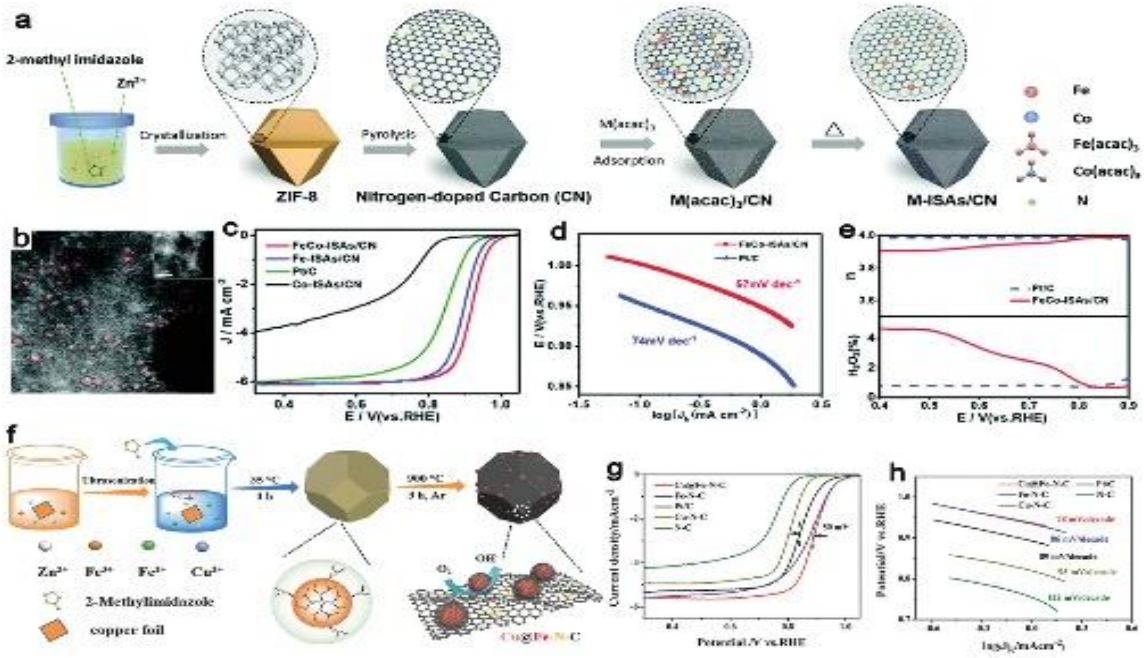

Figure 2.2 Atom-pair-based M–N–C electrocatalysts. a) Schematic illustration for the preparation of Fe–Co–N–C. b) Aberration-corrected scanning transmission electron microscopy (AC-STEM) image of Fe–Co–N–C. c) ORR polarization curves of FeCo-based electrocatalysts and commercial Pt/C in 0.1 m KOH solution. d) Corresponding Tafel plots obtained by RDE polarization curves. e) H_2O_2 yield and electron transfer

`

number plots of Fe–Co–N–C and Pt/C from 0.4 to 0.9 V (vs RHE). f) Schematic of the synthesis procedure of Cu–Fe–N–C [13].

2.2.3 ZIF derived Fe–N–C Electrocatalysts

Due to their higher catalytic performance in severe acidic conditions, Fe–N–C structures have been deemed amongst the most prospective ORR electrocatalysts among the many described M–N–C electrocatalysts. Active catalytic sites for ORR catalysis are frequently identified as Fe–Nx in carbon matrices. High-temperature pyrolyzing precursors including Fe and N components are inevitably involved in recently described Fe–N–C electrocatalysts. During heat pyrolysis, however, Fe atoms agglomerates and eventually develop less-active Fe-based complexes or nanoparticles enclosed in carbon matrixes, that are difficult to remove and so substantially limit the synthesis of catalytically active Fe–Nx in high density [14]. Furthermore, due to the sheer number of Fe–Nx getting coated by graphitic carbon matrix, which substantially lowers the catalytic performance of the Fe–N–C electrocatalysts, elevated pyrolysis may lead to a decrease availability to engage in the ORR process [15].

A variety of approaches have been used to improve the catalytic efficiency of Fe–N–C. The curved design of the Fe–N–C electrocatalysts has been created utilizing SiO_2-coating and pre - heating processes of Nanoparticle (Figure 2.3a), that significantly fuels the growth of exposed Fe–Nx and improves the mass transfer of the catalysts' layer. Moreover, atomic modification and structural containment can augment the Activity and stability of Fe–N–C electrocatalysts by loading P and S into the ZIF-precursors. Lately, catalysts comprised of a single iron atom anchored on an N, P, and S co-doped porous carbon polyhedron demonstrated remarkable ORR functionality. Nevertheless, Fenton-like interactions among Fe^{2+} and H_2O_2, that generate active free radicals, are a serious concern, as they are likely to induce electrocatalyst performance degradation and organic ionomer degradation within electrodes [16].

`

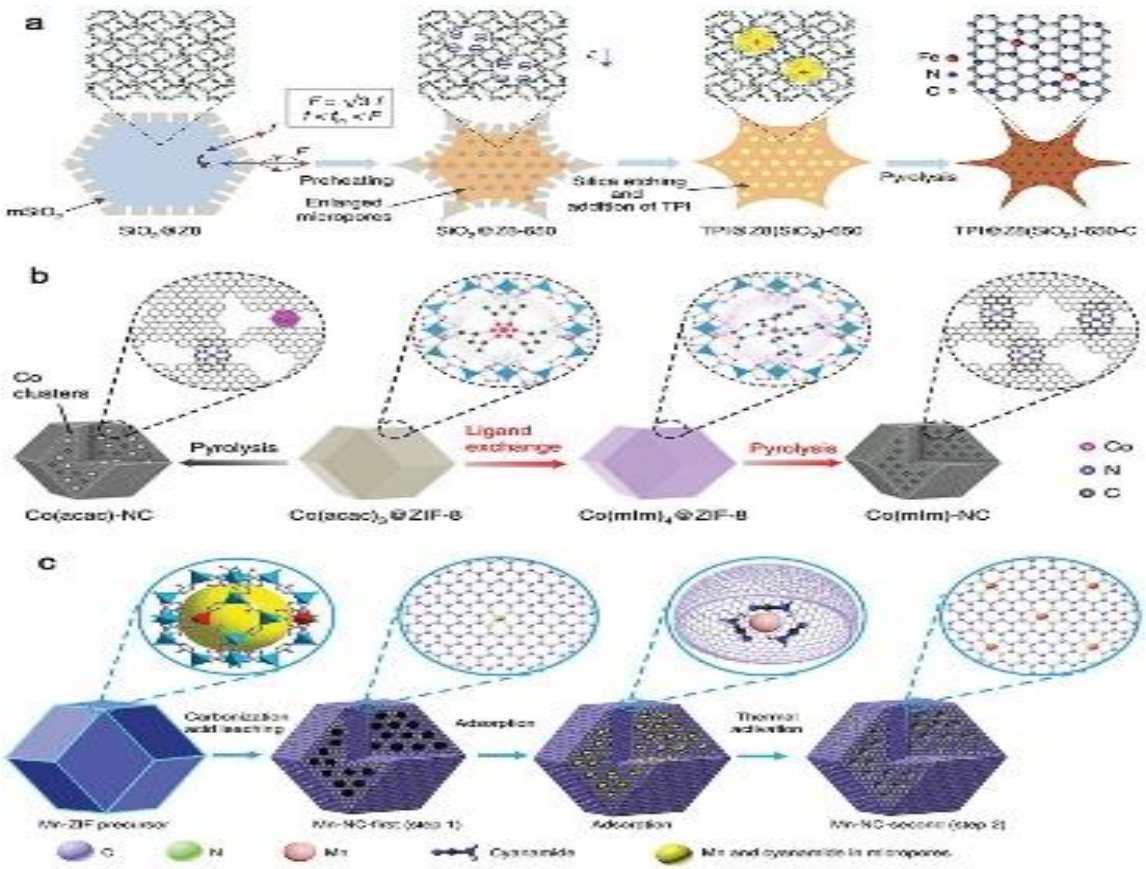

Figure 2.3 Fe–, Co–, and Mn–N–C electrocatalysts. a) The synthetic process of TPI@Z8 (SiO_2)-650-C by silica coating, preheating, etching silica off, absorbing TPI, and carbonization. b) A two-step encapsulation and ligand-exchange approach effectively introduces Co–N_4 complexes into the ZIF-8 micropores to synthesize Co–N–C. c) A two-step doping and adsorption approach to synthesize Mn–N–C [16].

2.3 Transition-Metal-Based Materials

2.3.1 Metals and Alloys

Cobalt was largely considered as being the most frequently utilized bifunctional ORR/OER active material. As oxygen electrocatalysts, metal and metallic alloy nanostructures made from carbon nanoparticles have been extensively explored. Figures 2.4a, b show Tem analysis of NiCo alloy nanoparticles sprayed on nanotubes. Polymer fibres containing metallic ions were created via spin coating. While the metal ions were being transformed to metallic alloys, the fibres were all being heat treated over N_2

`

isolation. Figure 2.4b depicts lattice fringes identical to the lattice fringes of various aspects in metallic Ni and Co. The ORR and OER behaviors of catalysts with varying concentrations of NiCo compositions in 0.10 M KOH are shown in Figures 2.4c, d. The best catalytic performance gives an ORR current density of 3.0 mA cm^{-2} at a potential of 0.81 V (the half-wave potential is 0.80 V) and an OER current density of 10 mA cm^{-2} at a potential of 1.76 V. The XPS examinations of Co and Ni atoms before and after OER investigations are depicted in Figure 2.4e.f. Co^{2+} and Ni^{2+} were identified on the catalyst's surface prior to electrochemical studies, and the metal atoms were oxidized to higher oxidation state following electro catalysis, indicating that metal (oxy) hydroxides constitute a significant proportion of the catalyst's functionality [14].

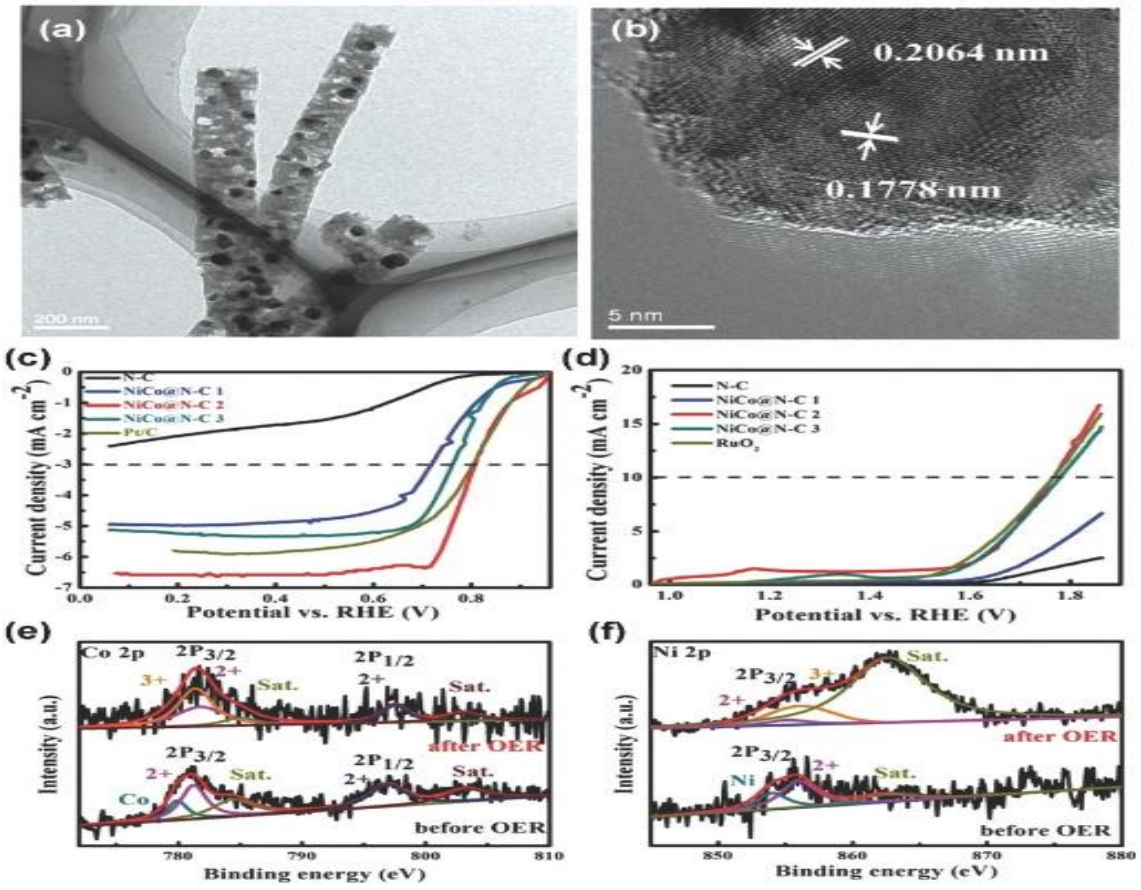

Figure 2.4 NiCo alloy material for bifunctional oxygen electrocatalysis. a) TEM and b) HRTEM images of NiCo alloy nanoparticles decorated on carbon nanofibers. c) ORR and d) OER LSV plots in O2-saturated 0.10 M KOH solution at the scan rate of 10 mV s−1. e) Co 2p and f) Ni 2p XPS spectra before and after OER electrocatalysis [14].

`

2.3.2 Transition Metal Compounds

Transition metal complexes like oxides, hydroxides, sulphides, and phosphides form a new family of bi - functional electrocatalysts. One of the very first compounds to be examined were metal oxides. Bifunctional oxygen electrocatalysts have been identified in spinels, perovskites, and other metal oxides. Reaction rates must first be discovered for the logical design of oxygen electrocatalysts. Xu and coworkers provided a criterion to evaluate activity employing spinel materials as an example. There appear to somehow be two types of metal sites in spinel-type materials, as seen in Figure 2.5a: tetrahedral sites and octahedral sites. The d-orbitals of metallic ions with octahedral coordination are separated into low-lying t_2g excited state and high-lying e.g. electron shells. Whenever orbitals connect to oxygen, they directly link to oxygen, leading to a huge spatial overlap including an O_2p orbital and a strong chemical connection. As a consequence, octahedral metal ions in spinel materials are considered active sites for oxygen electrocatalysis, and orbital occupancy can be utilized as a descriptor of activity. The concentration of metal ions at the octahedral site can be controlled by optimising the synthesizing environment and the type of metal ions, for instance. Figure 2.5b, c show volcanic plots of ORR and OER activity vs occupancy. The theoretical predictions for the volcanic plots (grey dotted line) were generated from past investigations and are consistent with the empirical data. As a result, the octahedral coordination can be identified as the catalytic site of spinel type oxygen electrocatalysts [15].

`

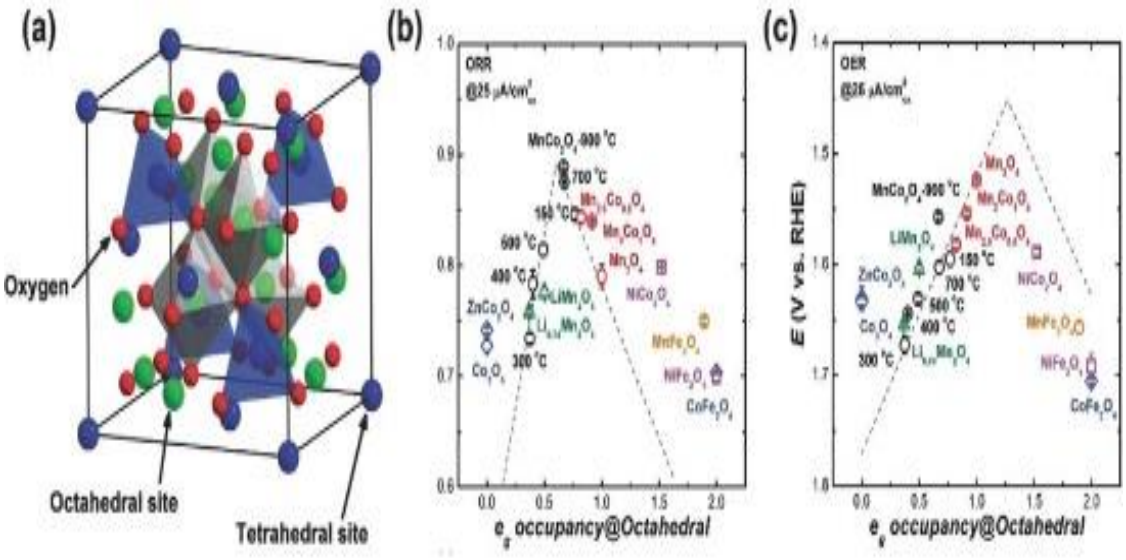

Figure 2.5 Active site identification for spinel-type oxygen electrocatalysts. a) Schematic of the spinel crystal structure. b) ORR and c) OER volcano plots with the activity as a function of e.g. occupancy of the active element at octahedral site [15].

Require a good understanding techniques are utilized to adjust the electrical configuration of the active metal sites in order to achieve the best electrocatalytic properties. Combining many metal ions together into single catalyst is a typical method for achieving the best catalytic properties. As a consequence, the advantages of different active locations can be integrated. Various metals ions' electrical configurations can interplay, leading in a complex formation. Amorphous bimetallic FeCo nano particles anchored on N-doped reduced GO (NrGO) were produced by Chen et al. [21] as both a bifunctional ORR and OER electrocatalyst. FeCoOx/NrGO catalysts with varying Fe/Co elemental proportions were generated by varying the type and concentration of the substrates. OER Linear sweep plots and Tafel plots of catalysts having varied a values tested in 1.0 M KOH are shown in Figures 2.6a, b. As per the overview of $E_{1/2}$ and Tafel plots, Fe0.5Co0.5Ox/NrGO has the highest OER activity (Figure 2.6c). The bifunctional properties of Fe0.5Co0.5Ox/NrGO were measured in 0.10 M KOH solution (Figure 2.6d). This FeCo oxide catalyst has such a small potential difference ($E = E_{10} \times E_3$) of 0.78 V, that is lower

`

than that of the IrO_2 and Pt/C composite catalyst. Transition metal compound cation control enabled effective bifunctional oxygen electrocatalysis [16].

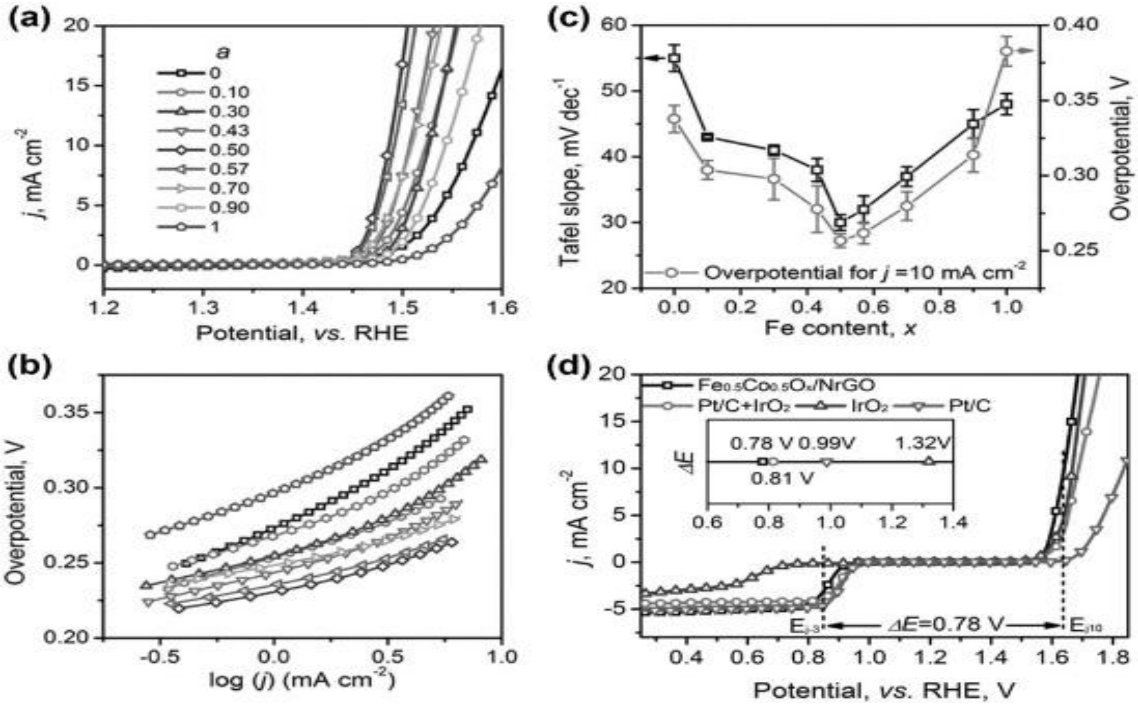

Figure 2.6 Cation regulation in bimetallic oxide electrocatalysts. a) OER LSV plots and b) Tafel plots of FeCo1-aOx/NrGO catalysts with different a values tested in 1.0 M KOH. The scan rate is 5 mV s−1 for LSV tests, and 0.2 mV s−1 for Tafel plot measurements. c) Summary of Tafel plots and the overpotential for 10 mA cm−2 current density at different a values. d) ORR and OER LSV plots of Fe0.5Co0.5Ox/NrGO and precious metal electrocatalysts. The ORR tests were carried out in O2-saturated 0.10 M KOH [16].

2.3.3 Composites of Transition-Metal-Based Materials

There are numerous linkages in composite electrocatalysts containing two or even more building units. The particular sequence of construction features can aid in improving catalytic performance. Efficient bifunctional electrocatalysts have been reported employing a variety of two or more different materials, comprising metal/oxide, oxide/oxide, sulfide/sulfide, and others. Guo et al. demonstrated a NiO/CoN composite catalyst synthesized by heating $NiCo_2O_4$ in an Ammonia atmosphere, with a firmly connected nanointerface between NiO and CoN nanostructures. Figure 2.7a depicts a TEM image of NiO/CoN, while Figure 2.7b depicts the HRTEM picture of the nanointerface (Figure 2.7b). The NiO/CoN compound possesses a disorganized localized

`

atomic structure, according to the expanded X-ray absorption fine structure (EXAFS) characterisation (Figure 2.7c, d). Interfaces somewhere at highly coupled contact lead to outstanding bifunctional electrocatalytic performance. The NiO/CoN catalyst had an E_{10} of 1.53 V (1.0 M KOH) and an $E_{1/2}$ of 0.78 V (0.10 M KOH) (Figure 2.7e, f). This has been proven that surface design is important in boosting ORR and OER electrocatalytic properties [17].

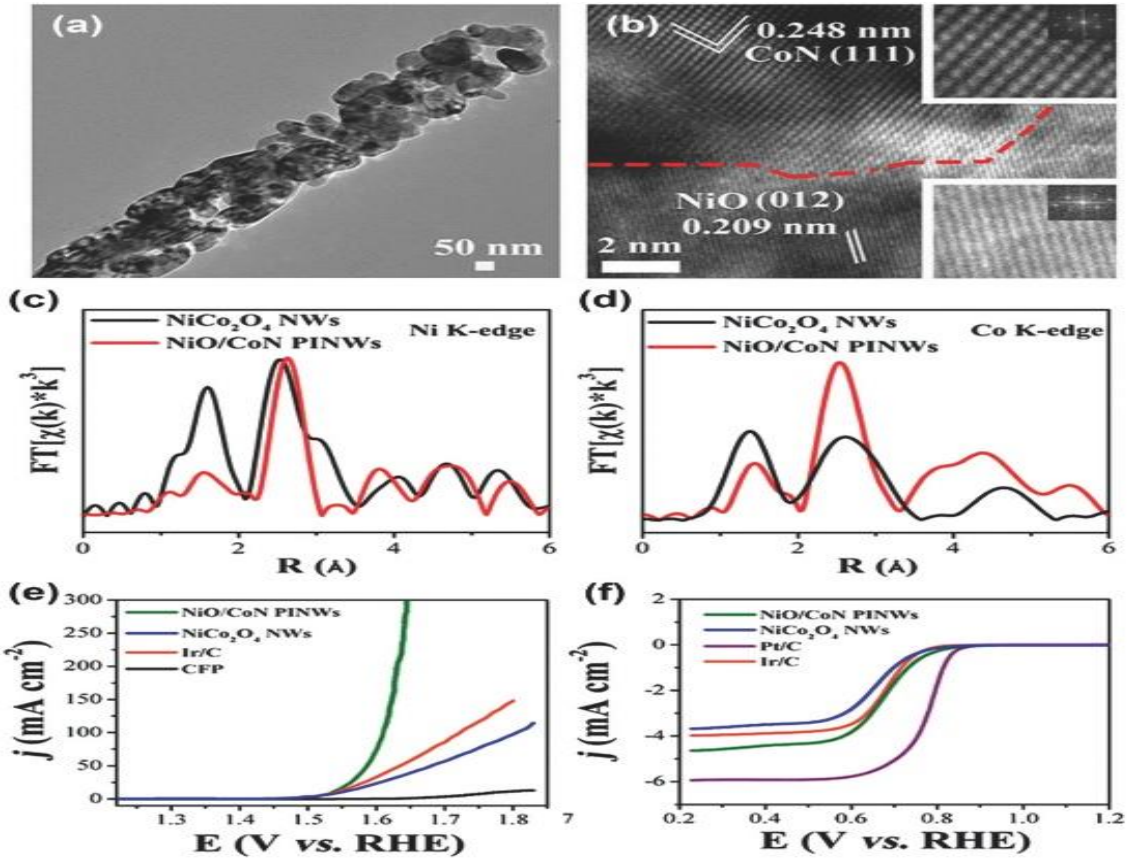

Figure 2.7 NiO/CoN for bifunctional electrocatalysis. a) TEM and b) HRTEM images. EXAFS spectra in R-space of NiO/CoN composite and $NiCo_2O_4$ at c) Ni K-edge and d) Co K-edge. e) OER and f) ORR LSV plots in 1.0 M KOH at a scan rate of 2.0 mV s^{-1} [17].

`

2.3.4 Atomically Dispersed Metal in Carbon Materials

Atomic dispersion at catalytic site can increase active site utilisation efficiency and chemical interactions with the support. Dopants metal atoms in composites can increase the inherent activity of metal-based active sites but also the electrical properties of carbon. In metal–doped carbon active sites, metal–Nx compositions are frequent [24]. In order to boost ORR and OER electrocatalytic properties, Zhi et al. used a single-site scattering of Fe–Nx particles in carbon substrates. To make the catalyst, Fe-containing ZIF-8 deposited on polypyrrole-coated graphene was exposed to high temperatures. The atomic dispersion of Fe–Nx ions was confirmed using a picture from a high-angle annular dark field scanning transmission electron microscope (HAADF-STEM) (Figure 2.8a). The XPS N 1s spectra also reported the existence of the Fe–Nx interaction (Figure 2.8b). This single-site iron-based catalyst exhibits a good bifunction ORR/OER activity of E = 0.775 V in 0.10 M KOH solution (Figure 2.8c) [18].

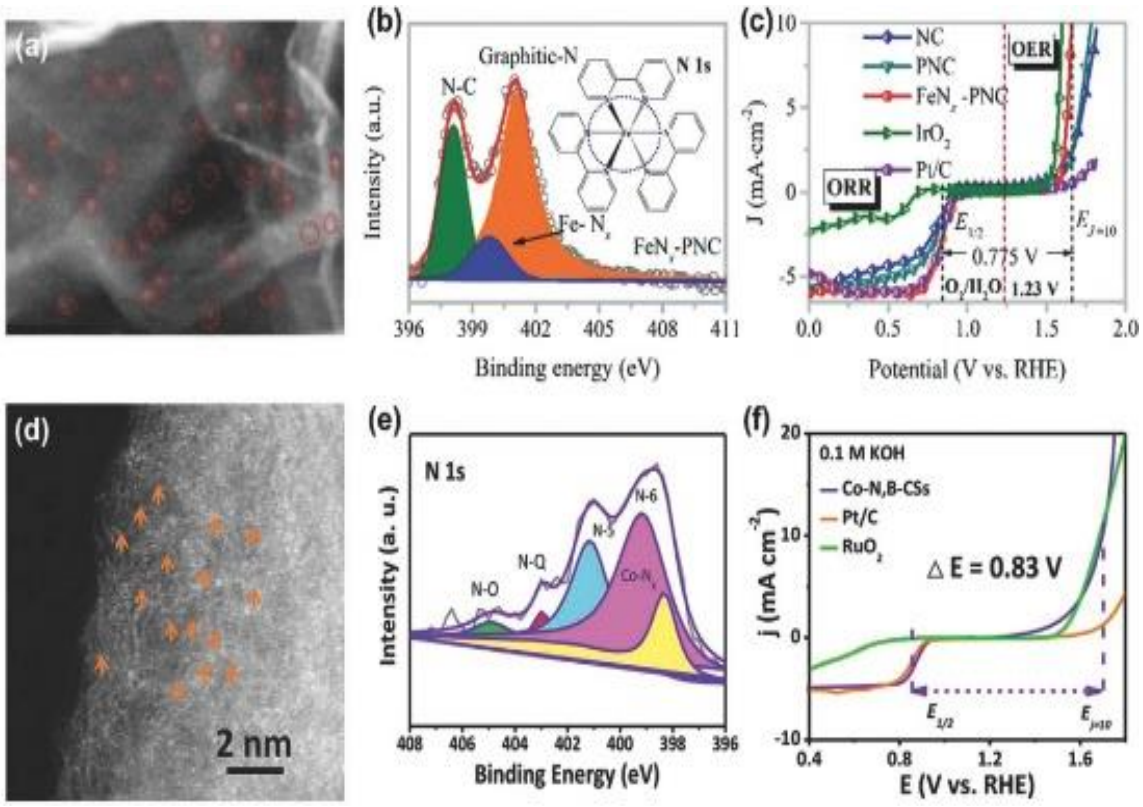

Figure 2.8 Atomically dispersed metal atoms on carbon scaffolds as electrocatalysts for ORR and OER. a) HAADF-STEM image of Fe–Nx species on graphene material. b) XPS N1s spectrum of FeNx-embedded carbon. c) ORR and OER LSV plots measured in

`

0.10 M KOH solution at 5.0 mV s^{-1}. d) HAADF-STEM image of atomic-scaled Co species on carbon sheets. e) High-resolution XPS spectrum of N 1s for Co/N–B-doped carbon. f) ORR and OER LSV plots in 0.10 M KOH solution with a scan rate of 5.0 mV s^{-1} [19].

The intrinsic activity of metal–Nx active sites can be controlled by altering the arrangement of atoms around the metal atoms. Boron-doped Co–N–C active sites in a bifunctional oxygen electrocatalyst have been reported recently. To remove Co nanoparticles, boric acid, ammonia, polyethylene glycol, and cobalt nitrate were mixed and heated up prior to getting acid cleaned. The atomic-scaled Co particles are evenly spread over carbon layers in the HAADF-STEM image in Figure 2.8d. The Co-Nx bonding can be detected in the XPS N 1s spectrum (Figure 2.8e), and the B 1s XPS spectrum verifies the formation of the B-C bond, B-N bond, and B-O bond, indicating a Co–Nx–By–C arrangement of the catalytic site [19].

`

Summary

The kinetics of the oxygen reduction reaction (ORR) and the many ORR pathways are discussed in this chapter. This chapter examined active materials for bifunctional electrocatalysis as well as other transition metal-based electrocatalysts.

`

References

[1] H. Meng, D. Zeng, and F. Xie, “Recent Development of Pd-Based Electrocatalysts for Proton Exchange Membrane Fuel Cells,” *Catalysts* , vol. 5, no. 3. 2015, doi: 10.3390/catal5031221.

[2] K. I. Ozoemena, “Nanostructured platinum-free electrocatalysts in alkaline direct alcohol fuel cells: catalyst design, principles and applications,” *RSC Adv.*, vol. 6, no. 92, pp. 89523–89550, 2016, doi: 10.1039/C6RA15057H.

[3] A. Damjanovic, M. A. Genshaw, and J. O. Bockris, “The Mechanism of Oxygen Reduction at Platinum in Alkaline Solutions with Special Reference to H[sub 2]O[sub 2],” *J. Electrochem. Soc.*, vol. 114, no. 11, p. 1107, 1967, doi: 10.1149/1.2426425.

[4] A. Damjanovic, D. B. Sepa, and M. V Vojnovic, “New evidence supports the proposed mechanism for O2 reduction at oxide free platinum electrodes,” *Electrochim. Acta*, vol. 24, no. 8, pp. 887–889, 1979, doi: https://doi.org/10.1016/0013-4686(79)87013-9.

[5] E. H. Yu, U. Krewer, and K. Scott, “Principles and Materials Aspects of Direct Alkaline Alcohol Fuel Cells,” *Energies* , vol. 3, no. 8. 2010, doi: 10.3390/en3081499.

[6] W. Yuan, K. Scott, and H. Cheng, “Fabrication and evaluation of Pt–Fe alloys as methanol tolerant cathode materials for direct methanol fuel cells,” *J. Power Sources*, vol. 163, no. 1, pp. 323–329, 2006, doi: https://doi.org/10.1016/j.jpowsour.2006.09.005.

[7] Q. Wei, Y. Fu, G. Zhang, and S. Sun, “Rational design of carbon-based oxygen electrocatalysts for zinc–air batteries,” *Curr. Opin. Electrochem.*, vol. 4, no. 1, pp. 45–59, 2017, doi: https://doi.org/10.1016/j.coelec.2017.09.006.

[8] F. K. Kessler *et al.*, “Functional carbon nitride materials — design strategies for electrochemical devices,” *Nat. Rev. Mater.*, vol. 2, no. 6, p. 17030, 2017, doi: 10.1038/natrevmats.2017.30.

`

[9] X. Liu and L. Dai, “Carbon-based metal-free catalysts,” *Nat. Rev. Mater.*, vol. 1, no. 11, p. 16064, 2016, doi: 10.1038/natrevmats.2016.64.

[10] W. Lei *et al.*, “Two-Dimensional Phosphorus-Doped Carbon Nanosheets with Tunable Porosity for Oxygen Reactions in Zinc-Air Batteries,” *ACS Catal.*, vol. 8, no. 3, pp. 2464–2472, Mar. 2018, doi: 10.1021/acscatal.7b02739.

[11] C. Tang and Q. Zhang, “Nanocarbon for Oxygen Reduction Electrocatalysis: Dopants, Edges, and Defects,” *Adv. Mater.*, vol. 29, no. 13, p. 1604103, Apr. 2017, doi: https://doi.org/10.1002/adma.201604103.

[12] C. Tang *et al.*, “Topological Defects in Metal-Free Nanocarbon for Oxygen Electrocatalysis,” *Adv. Mater.*, vol. 28, no. 32, pp. 6845–6851, Aug. 2016, doi: https://doi.org/10.1002/adma.201601406.

[13] H.-F. Wang, C. Tang, B. Wang, B.-Q. Li, X. Cui, and Q. Zhang, “Defect-rich carbon fiber electrocatalysts with porous graphene skin for flexible solid-state zinc–air batteries,” *Energy Storage Mater.*, vol. 15, pp. 124–130, 2018, doi: https://doi.org/10.1016/j.ensm.2018.03.022.

[14] Y. Fu *et al.*, “NiCo Alloy Nanoparticles Decorated on N-Doped Carbon Nanofibers as Highly Active and Durable Oxygen Electrocatalyst,” *Adv. Funct. Mater.*, vol. 28, no. 9, p. 1705094, Feb. 2018, doi: https://doi.org/10.1002/adfm.201705094.

[15] M. Zhang, Q. Dai, H. Zheng, M. Chen, and L. Dai, “Novel MOF-Derived Co@N-C Bifunctional Catalysts for Highly Efficient Zn–Air Batteries and Water Splitting,” *Adv. Mater.*, vol. 30, no. 10, p. 1705431, Mar. 2018, doi: https://doi.org/10.1002/adma.201705431.

[16] S. Feng, C. Liu, Z. Chai, Q. Li, and D. Xu, “Cobalt-based hydroxide nanoparticles @ N-doping carbonic frameworks core–shell structures as highly efficient bifunctional electrocatalysts for oxygen evolution and oxygen reduction reactions,” *Nano Res.*, vol. 11, no. 3, pp. 1482–1489, 2018, doi: 10.1007/s12274-017-1765-2.

[17] H. Li *et al.*, “Colloidal Cobalt Phosphide Nanocrystals as Trifunctional Electrocatalysts for Overall Water Splitting Powered by a Zinc–Air Battery,” *Adv.*

`

Mater., vol. 30, no. 9, p. 1705796, Mar. 2018, doi: https://doi.org/10.1002/adma.201705796.

[18] J. Lv *et al.*, "A photo-responsive bifunctional electrocatalyst for oxygen reduction and evolution reactions," *Nano Energy*, vol. 43, pp. 130–137, 2018, doi: https://doi.org/10.1016/j.nanoen.2017.11.020.

[19] X. Zhang, Z. Yang, Z. Lu, and W. Wang, "Bifunctional CoNx embedded graphene electrocatalysts for OER and ORR: A theoretical evaluation," *Carbon N. Y.*, vol. 130, pp. 112–119, 2018, doi: https://doi.org/10.1016/j.carbon.2017.12.121.

[20] H. Li *et al.*, "Colloidal Cobalt Phosphide Nanocrystals as Trifunctional Electrocatalysts for Overall Water Splitting Powered by a Zinc–Air Battery," *Adv. Mater.*, vol. 30, no. 9, p. 1705796, Mar. 2018, doi: https://doi.org/10.1002/adma.201705796.

[21] J. Lv *et al.*, "A photo-responsive bifunctional electrocatalyst for oxygen reduction and evolution reactions," *Nano Energy*, vol. 43, pp. 130–137, 2018, doi: https://doi.org/10.1016/j.nanoen.2017.11.020.

[22] X. Zhang, Z. Yang, Z. Lu, and W. Wang, "Bifunctional CoNx embedded graphene electrocatalysts for OER and ORR: A theoretical evaluation," *Carbon N. Y.*, vol. 130, pp. 112–119, 2018, doi: https://doi.org/10.1016/j.carbon.2017.12.121.

`

CHAPTER 3: SYNTHESIS AND CHARACTERIZATION TECHNIQUES

3.1 Synthesis Method

Many strategies have been implemented in the lab for the effective development of the catalyst material. Some of them necessitate the use of sophisticated equipment, while others are conducted without it. The desirable size, appropriate surface qualities, and type of material involved (semiconductors, metals, polymers, ceramics, etc.) all influence the catalyst synthesis procedure used to produce the needed NPs. These approaches have been studied and developed in order to improve our catalyst's yield, structural characteristics, and purity. Some of these strategies are detailed below:

3.1.1 Solvothermal Synthesis

It is a method for producing a variety of materials such as semiconductors, metals, polymers, and ceramics. The technique includes a solvent at medium to high pressure (usually within 1 atm to 10,000 atm) and temperature (ranging from 100 °C to 1000 °C), which assists in the contact of substrates during synthesis. The procedure is known as the "hydrothermal process" if water is employed as the solvent. The supercritical water temperature (374 °C) is frequently maintained during the hydrothermal synthesis method. This process can be used to synthesize thin films, single crystals, bulk powders, and nanocrystals in a range of morphologies. Furthermore, the regulation of chemical concentration, solvent super saturation, and kinetic control arrange the formation (rod (2D), spheres (3D), and wires (1D) of crystals. It can be utilized to create thermodynamically stable, stationary structures incorporating unique elements that are difficult to create using traditional synthetic pathways. Because nanocrystals occupied 80% of the literature in the last decade, this review will focus on some recent advancements, such as the solvothermal method and nanocrystalline materials [1].

3.1.2 Hydrothermal Synthesis

This procedure is used to develop materials that require unique circumstances to be developed. This technique also aids in the modulation of the material's shape,

`

morphology, and other qualities. This process is primarily used to produce metal oxides, halides, and composites that demand a certain temperature and pressure. This approach produces nanoparticles with distinct characteristics. This procedure usually involves the use of an autoclave unit that allows pressure and temperature to be regulated continuously. The capacity to manufacture a large number of nanoparticles with improved composition, size, morphology, and chemistry of surface at an affordable cost is the most important aspect of this technique [2].

3.1.3 Pyrolysis

In an inert, oxygen-free atmosphere, organic matter is converted into noncondensable gases, condensable liquids, and bio char or charcoal as a residual solid material during pyrolysis [3].

3.1.4 Carbonization

Carbonization is a thermal breakdown technique that gives carbon-containing waste from organic materials a second life while also eliminating the residue. The earliest primary way of creating liquids from coal is pyrolysis. It involves heating coal and capturing vaporized liquids, leaving a carbon residue deficient in hydrogen. Aside from the minimal amount of liquid recovered (less than 20%), the combination of chemicals and water pollution results in a subpar output. Carbonization is generally utilized to produce a carbonaceous residue known as coke, while organic matter is destroyed at high temperatures and the distillate is extracted at the same time. ZIF is carbonized to make nano porous carbon and carbon nanotubes [4].

3.2 Characterization Techniques

3.2.1 X-Ray Diffraction (XRD)

This is a frequent and useful material characterization technique that offers insight about the morphology, components, and crystallite size of the material. It works by using X-rays that travel through the material at an angle towards the source of the radiation. The intensity is measured and the diffraction angle is determined. The number of radiations that deflected from a certain plane on a material at an angle provides information about its structure and shape.

`

High-energy electrons are focused on a metal target by an X-ray tube, which produces X-rays. Destructive interference of a crystalline sample with monochromatic X-rays produces the X-rays seen on the screen. The output from XRD is plotted with intensity on the y-axis and 2θ on the x-axis. θ is the angle at which X-rays strike the sample. A phase shift in rays occurs as a result of the existence of changing lattice spacing (Figure 3.1) in the material, and specific peaks develop. It is understandable using Bragg's law;

$$2d \sin\theta = n\lambda \qquad \text{(eq. 3.1)}$$

Where;

d= is the interlayer distance

λ= is the wavelength

n= is total number of layer under observation

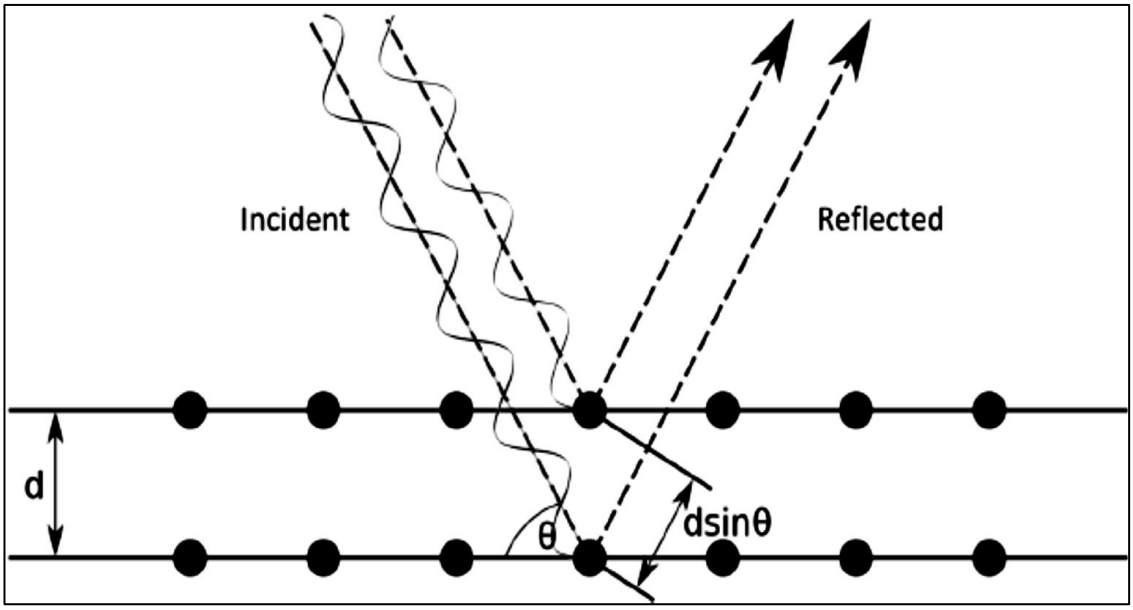

Figure 3.1 The Bragg's Law

The direction of anticipated diffraction is determined by the shape and size of the material's unit cell. The diffracted wave intensities are influenced by the arrangement of the atoms in the crystal structure. Several structures are composed of tiny crystallites arranged across all directions. This is known as polycrystalline powder or aggregate. Whenever an X-ray beam is directed at a material with lightly concentrated crystallites, it

`

will see all accessible interatomic planes. All of the available diffraction peaks from the substance will be recognised if the experimental angle is changed scientifically [5].

3.2.2 Scanning Electron Microscopy

The scanning electron microscope (SEM) displays a broad spectrum of signals on the solid surface of the material by concentrating a high-energy beam of electrons. As demonstrated in Figure 3.2, high-energy electrons pierce the substance and exit through the other end. Signals of electron beam and specimen interactions will disclose information about the material such as chemical composition, crystalline nature, surface morphology (texture), and material alignment. A 2-dimensional image is formed in different applications that illustrates spatial changes in these characteristics, and numbers are recorded over a specific area of the specimen surface. Simple SEM techniques (magnifications ranging from 20X to roughly 30,000X, 3-D resolution of 50 to 100 nm) are being used to discern areas ranging in size from about 1 cm to 5 microns in width. This technique is only useful for detecting chemical compounds (by EDS), crystal orientations (by EBSD), and crystalline structures in a semi-quantitative or qualitative manner. The SEM is capable of analyzing a specific area or spot on the reference material. It has a design and layout that is quite similar to the EPMA, and the two devices have a lot of features in common [6].

`

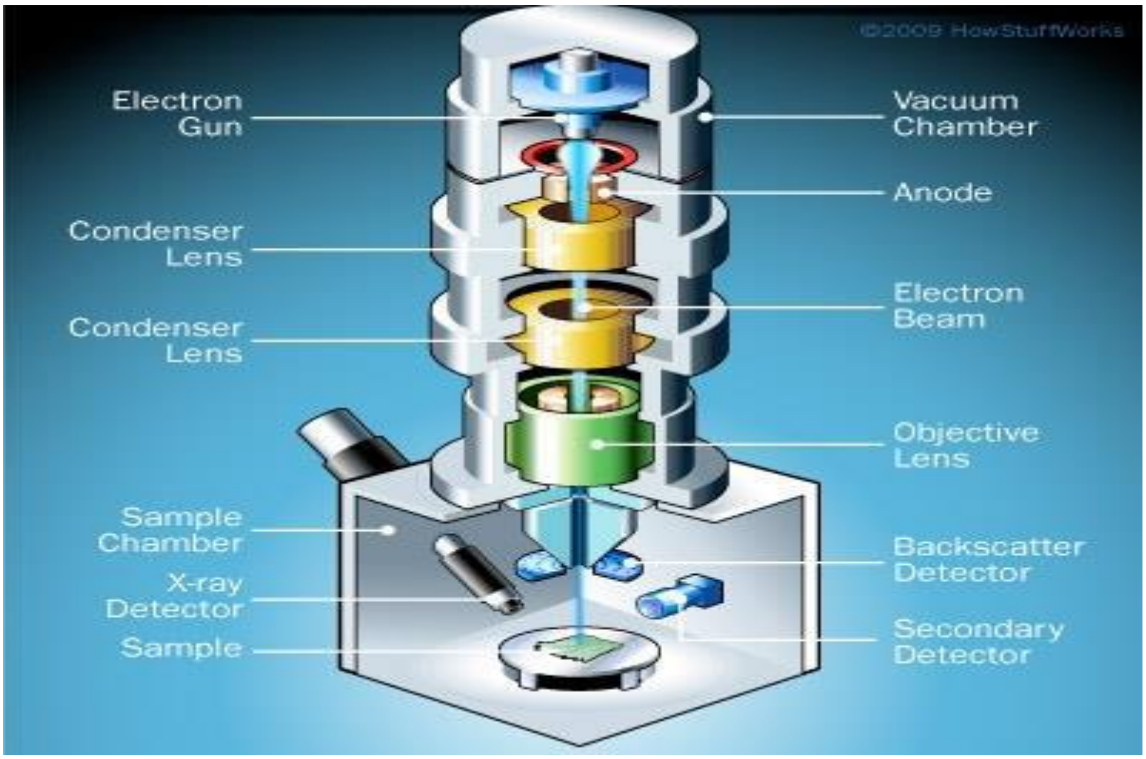

Figure 3.2 Illustration of how SEM works

3.2.3 Energy Dispersive X-ray Spectroscopy (EDX)

EDS is a method of elemental analysis that is used to determine the quantity of specific elements contained in a nanoparticle. This method provides the number of elements at a specific position but does not provide the total amount of each element. It's frequently used in conjunction with SEM or TEM to provide a nanoscale picture of nanoparticles, and EDS analyses that nanostructure. EDS became a commercial product in the early 1970s, quickly surpassing WDS in popularity. As there are no moving parts in the EDS, unlike the rotation detector in the WDS, the overall structure is fairly basic. As shown in Figure 3.3, the detector receives the X-ray energy signal across all consecutive elements in the sample at the very same time, as opposed to receiving signals from X-ray energy one by one, making EDS systems comparatively rapid. The typical energy dispersion frequency is roughly 150–200 eV, which is lower than what WDS can achieve. The lightest component detected is O (Z = 8), not C (Z = 6). However, key advantages such as low cost and rapid analysis outweigh these drawbacks [7].

`

The EDS band is a chart that shows the relationship between the intensity of X-rays and their related energies. Since both M or L lines of heavy elements and K lines of light elements are visible in this array, both light and heavy elements can be seen in a spectrum ranging from 0.1 to 10-20 keV.

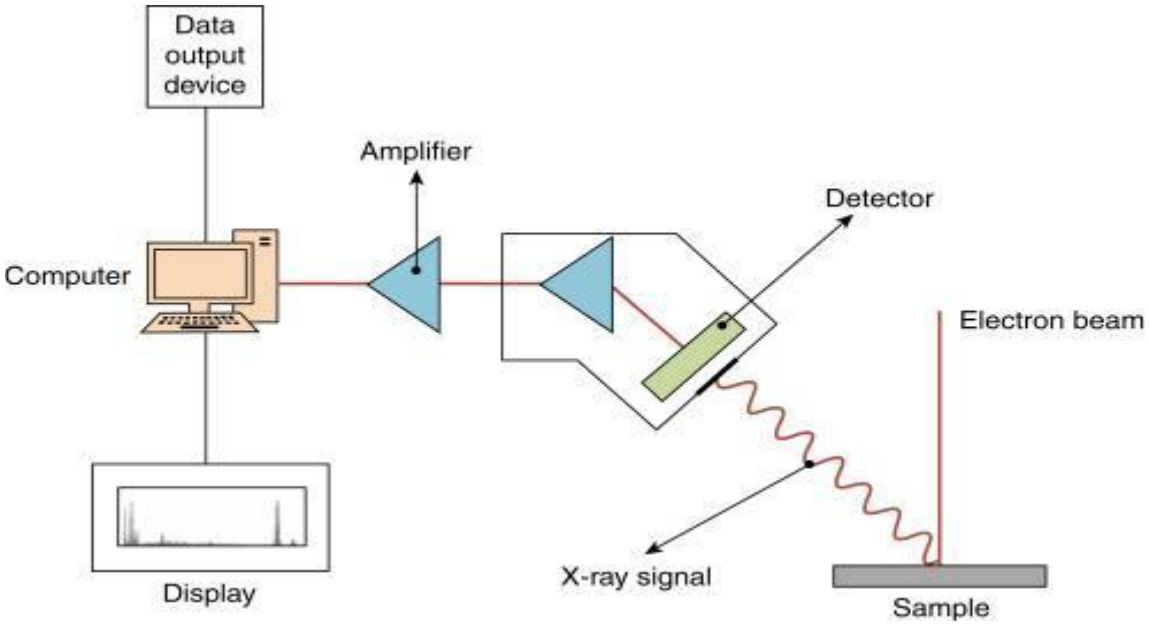

Figure 3.3 Illustration of EDX

3.2.4 Thermo-Gravimetric Analysis

In a controlled environment, thermogravimetric analysis (TGA) analyses weight losses in a material as a function of temperature. Thermal stability, volatile quantity, humidity, organic binder in a substance, and the percent composition of components in a compound are some of the most common applications of this characterization method. In a given gas environment, such as Ar, air, or another gas, the temperature is progressively increased from zero to the desired end temperature. The contents of the sample begin to evaporate as the temperature rises. Moisture is typically the first substance to be removed from a sample, resulting in a change in weight. Throughout the process, this mass is continuously monitored on a mass balance located outside the reactor (Fig. 3.4). Other volatile substances, such as organic residues, begin to escape once the moisture has evaporated. The temperature at which the material begins to breakdown, which is the primary point

`

on the curve, can be used to determine the sample's stability. The line then abruptly drops, resulting in a significant material loss. The breakdown temperature determines the material's stability. The weight of the material is plotted versus time or temperature to show the thermal variations in the material, such as solvent loss, water loss during hydration, and material degradation. The final mass residue is recorded at the end of the process, and the overall loss in weight is calculated [8].

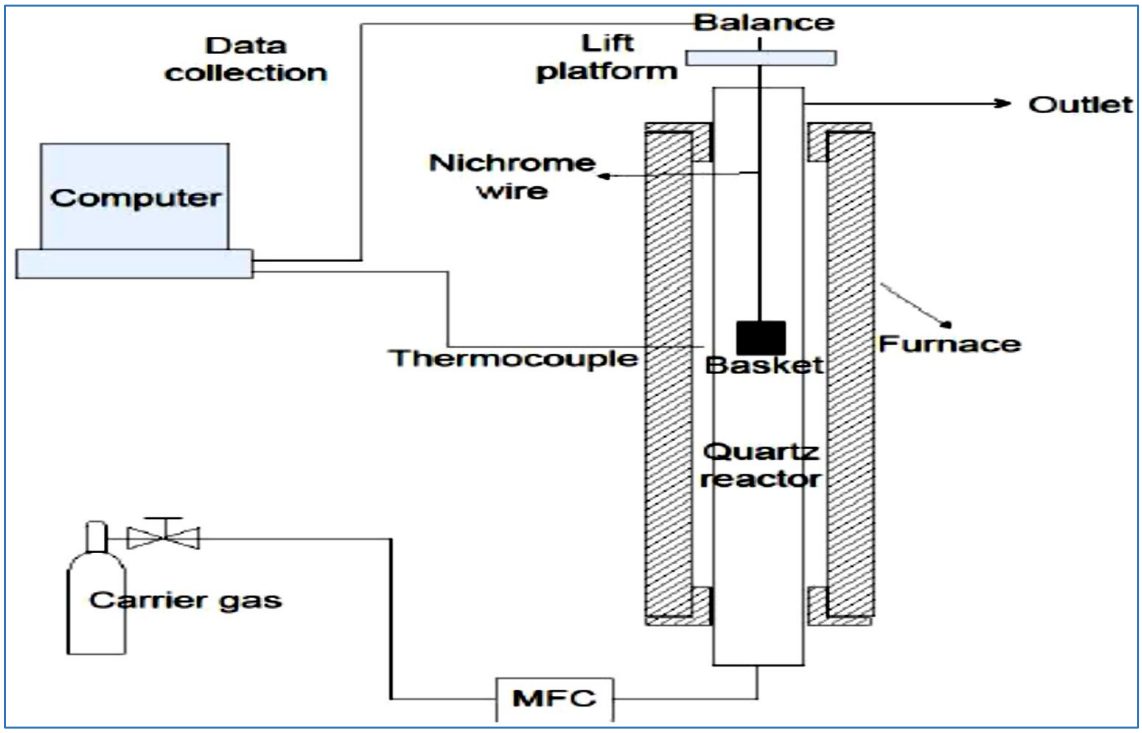

Figure 3.4 Schematic of TGA

3.2.5 X-ray photoelectron spectroscopy (XPS)

X-ray photoelectron spectroscopy (XPS) is a potent, surface-sensitive technique used to determine the chemical composition of materials. It is also known as electron spectroscopy for chemical analysis (ESCA). It is performed by exposing a sample to X-rays to excite the material and then evaluating the energy of the generated photoelectrons. MgK (1253.6 eV) or AlK (1486.6 eV) are commonly employed as soft X-ray sources. Incident X-rays can penetrate from 1 to 10 nm in solids based on the atom matrix in the structure of the substance [9].

`

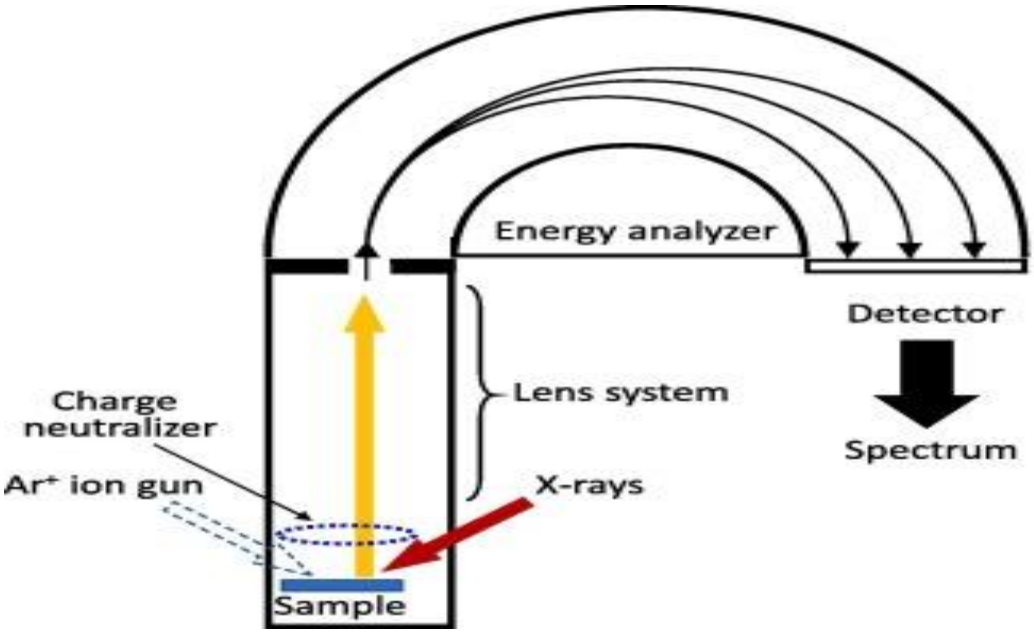

Figure 3.5 Schematic diagram of XPS

3.2.6 Transmission Electron Microscopy (TEM)

A high-energy electron beam (usually 100–400 keV) is compressed by magnetic lenses and is supposed to cross through an object under high vacuum in this approach. A consequent diffraction pattern can be formed by the transmitted beam and a number of diffracted beams, which is photographed on a fluorescent screen kept below the specimen. The diffraction pattern indicates the lattice spacing and symmetry of the structure under discussion. As an alternative, bright-field and dark-field scanning modes can be used to magnify the sample on the display monitor using either the transmitted or diffracted beams. This reveals the material's microstructural elements' size and shape. The atomic structure of the material is depicted in detail in this high-resolution photograph. This can be accomplished by combining the transmitted and diffracted beams.

`

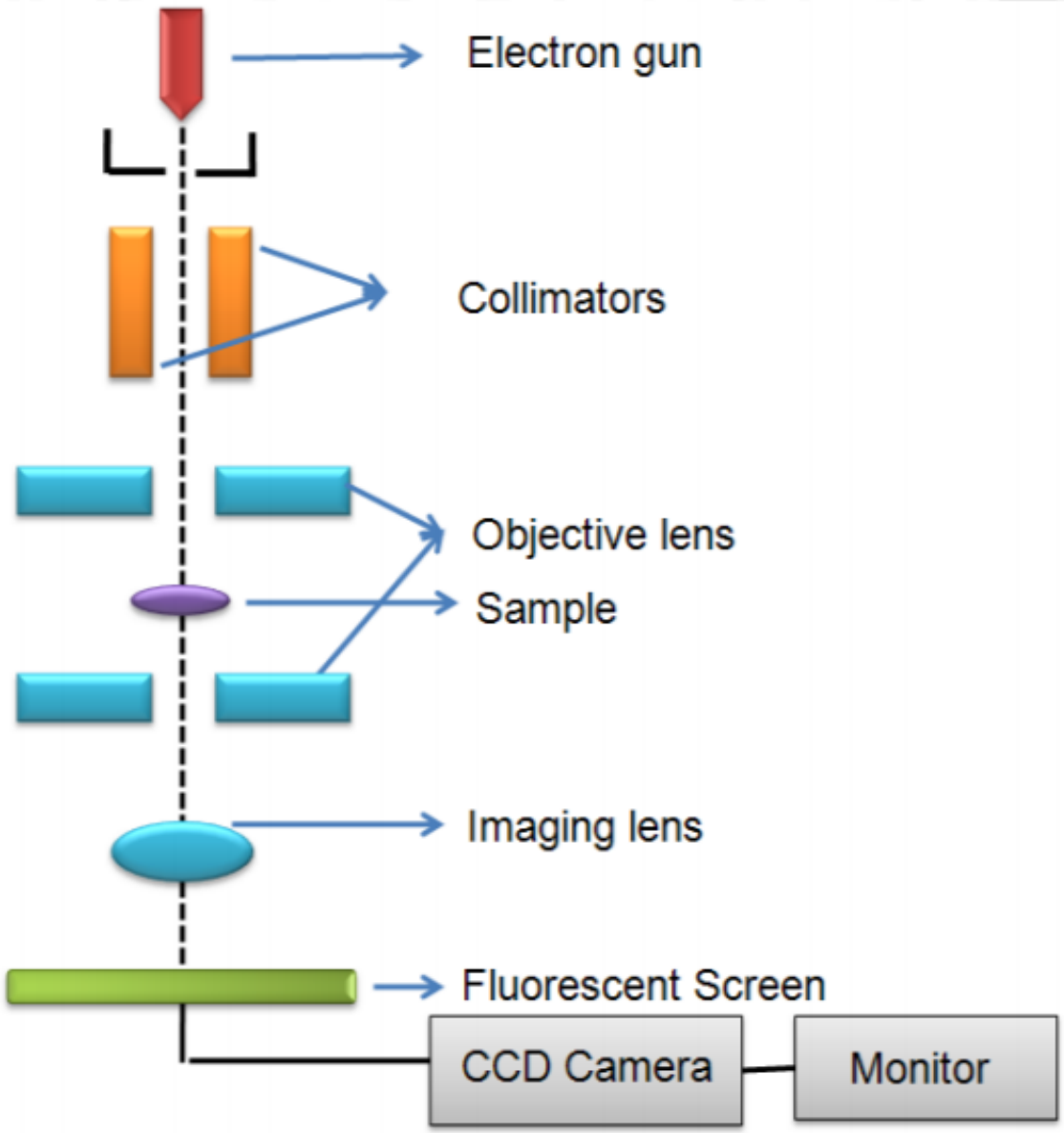

Figure 3.6 Functional diagram of TEM

3.3 Electrochemical Testing

To determine the electrochemical characteristics of the samples, we employed cyclic voltammetry, electrochemical impedance spectroscopy and linear sweep voltammetry among others.

3.3.1 Cyclic Voltammetry

Cyclic voltammetry (CV) is a well-known and widely used electrochemical technique for studying the redox reaction mechanisms of molecular species. It is beneficial to research chemical reactions triggered by electron transfer, which includes catalysis. The

`

workstation is run through a complete cycle in this electrochemical method. The software was used to apply the potential range across the two electrodes. Each run was assigned a scan rate, sample interval, and sensitivity, as well as multiple segments. One cycle is made up of two segments. As shown in Figure 3.6, cyclic voltammetry provides information on how current varies with voltage. When CV is conducted, electrons begin to flow from anode to cathode through an external circuit. A three-electrode setup with a beaker cell was employed for CV. Glassy carbon served as the working electrode, while platinum wire served as the counter electrode, and Ag/AgCl served as the reference electrode [10].

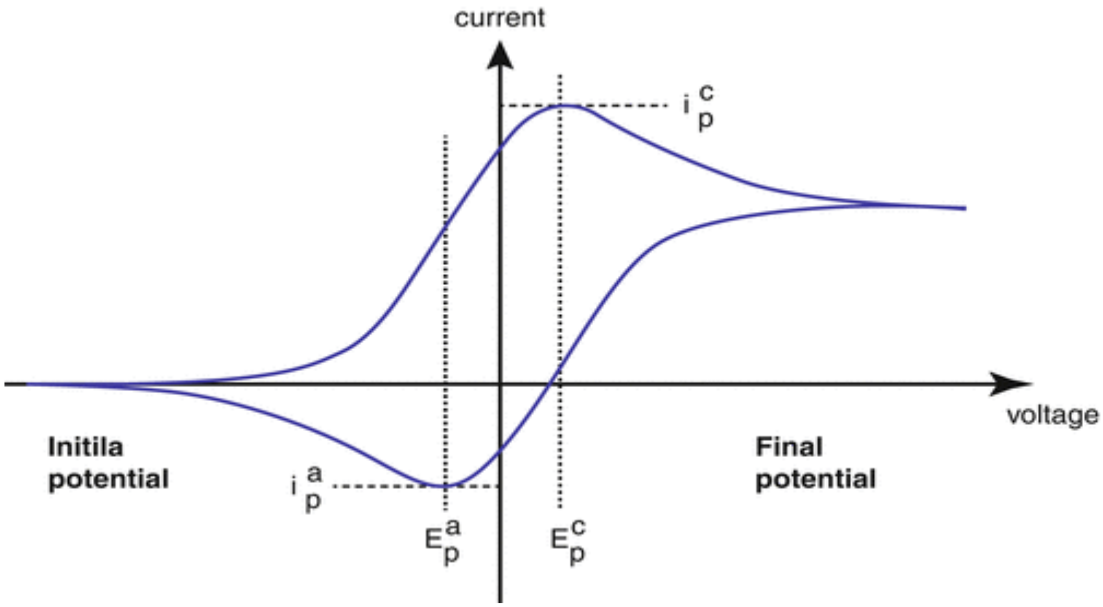

Figure 3.7 CV profile

3.3.2 Electrochemical Impedance Spectroscopy (EIS)

We can measure our system's resistance using this electrochemical workstation technique. This can involve electrolyte resistance, ohmic loss, and/or activation losses. The electrical resistance of a circuit element is the amount of current flow that it resists [11].

$$R=E/I$$

Ohm's law states that R is the resistance, which is described as the ratio of voltage (E) to current (I). This well-known law can only be applied to one circuit element, the ideal resistor.

The following are some of the characteristics of an ideal resistor:

`

• Ohm's Law applies to all voltage and current ranges.

• Resistance is not frequency dependent.

• The voltage going through a resistor as well as the AC current are in a single phase.

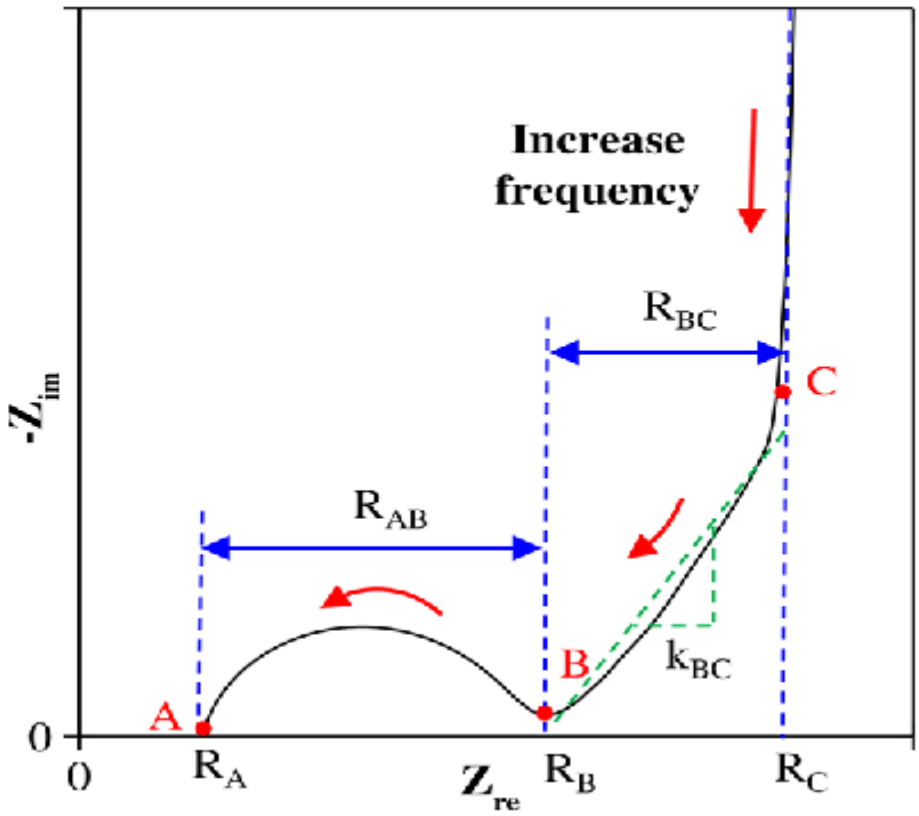

Figure 3.8 EIS Profile (Nyquist Plot)

3.3.3 Chronoamperometry

Chronoamperometry is an electrochemical technique that involves stepping the voltage of the working electrode and monitoring the resulting current from faradaic processes taking place at the electrode (induced by the potential step) as a function of time. After employing a suitable or double potential step to the working electrode of the electrochemical system, the functional connection between current response and time is determined. The ratio of peak oxidation current to peak reduction current can provide some information regarding the identification of the electrolyzed species. Chronoamperometry, like all pulsed approaches, produces large charging currents that, like any RC circuit, decrease

`

exponentially with time. The Cottrell equation describes the decline of the Faradaic current, which is caused by electron transfer events and is most typically the current component of interest. This decay is substantially slower for most electrochemical cells than the charging decay cells without a supporting electrolyte are notable examples. A three electrode arrangement is most typically utilized. Chronoamperometry has a higher signal-to-noise ratio than other amperometric techniques because the current is integrated over longer time intervals [12].

`

Summary

This chapter has covered various synthesis approaches for producing metal organic frameworks. Material characterization analytical instruments such as XRD, SEM, TGA, XPS, and EIS have been briefly presented in terms of working principles and how these analytical methods might benefit our research.

`

References

[1] B. Zhang et al., “Solvent determines the formation and properties of metal–organic frameworks,” RSC Adv., vol. 5, no. 47, pp. 37691–37696, 2015, doi: 10.1039/C5RA02440D.

[2] I. U. Khan et al., “Economical, environmental friendly synthesis, characterization for the production of zeolitic imidazolate framework-8 (ZIF-8) nanoparticles with enhanced CO2 adsorption,” Arab. J. Chem., vol. 11, no. 7, pp. 1072–1083, 2018, doi: https://doi.org/10.1016/j.arabjc.2018.07.012.

[3] X. Wen, Q. Zhang, and J. Guan, “Applications of metal–organic framework-derived materials in fuel cells and metal-air batteries,” Coord. Chem. Rev., vol. 409, p. 213214, 2020, doi: https://doi.org/10.1016/j.ccr.2020.213214.

[4] K. Li et al., “Bimetallic ZIF derived Co nanoparticle anchored N-doped porous carbons for an efficient oxygen reduction reaction,” Inorg. Chem. Front., vol. 7, no. 4, pp. 946–952, 2020, doi: 10.1039/C9QI01487J.

[5] M. Gonon, “Case Studies in the X-ray Diffraction of Ceramics,” M. B. T.-E. Of M. T. C. and G. Pomeroy, Ed. Oxford: Elsevier, 2021, pp. 560–577.

[6] S. Wen, J. Liu, and J. Deng, “Chapter 3 - Methods for the detection and composition study of fluid inclusions,” S. Wen, J. Liu, and J. B. T.-F. I. E. in F. of S. M. Deng, Eds. Elsevier, 2021, pp. 27–68.

[7] F. U. Kosasih, S. Cacovich, G. Divitini, and C. Ducati, “Nanometric Chemical Analysis of Beam-Sensitive Materials: A Case Study of STEM-EDX on Perovskite Solar Cells,” Small Methods, vol. 5, no. 2, p. 2000835, Feb. 2021, doi: https://doi.org/10.1002/smtd.202000835.

[8] S. Loganathan, R. B. Valapa, R. K. Mishra, G. Pugazhenthi, and S. Thomas, “Chapter 4 - Thermogravimetric Analysis for Characterization of Nanomaterials,” in Micro and Nano Technologies, S. Thomas, R. Thomas, A. K. Zachariah, and R. K. B. T.-T. and R. M. T. for N. C. Mishra, Eds. Elsevier, 2017, pp. 67–108.

[9] M. H. Engelhard, T. C. Droubay, and Y. Du, “X-Ray Photoelectron Spectroscopy

`

Applications," J. C. Lindon, G. E. Tranter, and D. W. B. T.-E. of S. and S. (Third E. Koppenaal, Eds. Oxford: Academic Press, 2017, pp. 716–724.

[10] N. Elgrishi, K. J. Rountree, B. D. McCarthy, E. S. Rountree, T. T. Eisenhart, and J. L. Dempsey, "A Practical Beginner's Guide to Cyclic Voltammetry," J. Chem. Educ., vol. 95, no. 2, pp. 197–206, Feb. 2018, doi: 10.1021/acs.jchemed.7b00361.

[11] C. L. C. Ellis, E. Smith, H. Javaid, G. Berns, and D. Venkataraman, "Chapter 6 - Ion Migration in Hybrid Perovskites: Evolving Understanding of a Dynamic Phenomenon," S. Thomas and A. B. T.-P. P. Thankappan, Eds. Academic Press, 2018, pp. 163–196.

[12] R. J. Mortimer, "Spectroelectrochemistry, Methods and Instrumentation," J. C. Lindon, G. E. Tranter, and D. W. B. T.-E. of S. and S. (Third E. Koppenaal, Eds. Oxford: Academic Press, 2017, pp. 172–177.

`

CHAPTER 4: METHODOLOGY

4.1 Chemical Reagents

Zinc nitrate hexahydrate (95%, Duksan), 2-methylimidazole (99%, Sigma Aldrich), Nickel nitrate hexahydrate (97%, Sigma Aldrich), Potassium hydroxide (86%, Sigma Aldrich), Iron nitrate nanohydrate (98%, Daejung), Melamine (99%, Daejung), methanol (99.9%, Merck), N, N-dimethylformamide (99.5%, Merck), Pt/C (10 wt% metal, Alfa Aesar), Nafion (5% w/w in water and 1-propanol, Ion Power), were used without any further purification.

4.2 Material Synthesis

4.2.1 Synthesis of Ni doped ZIF-8

As reported [1], $Zn(NO_3)_2.6H_2O$ (595 mg) and $Ni(NO_3)_2.6H_2O$ (4ll mg) was mixed in 15 m1 methanol and vortexed for 30 minutes in jar A to generate a homogeneous mixture. In flask B, 2-methylimidazole (657 mg) being saturated in 7.5 m1 of methanol as wel1 as vigorously agitated. The reaction mixture was again vigorously swirled at room temperature for 2 hours after becoming stirred into solution B. This mixture was taken inside a 50 ml Teflon-lined stainless-steel autoclave and hydrothermally treated at 120^{o}C for 4 hours. This same specimen was then extracted then subsequently rinsed with DMF and methanol. After that, it spent the night drying at 70°C inside a vacuum oven. The synthesis route's process chart is shown in Figure 4.1.

`

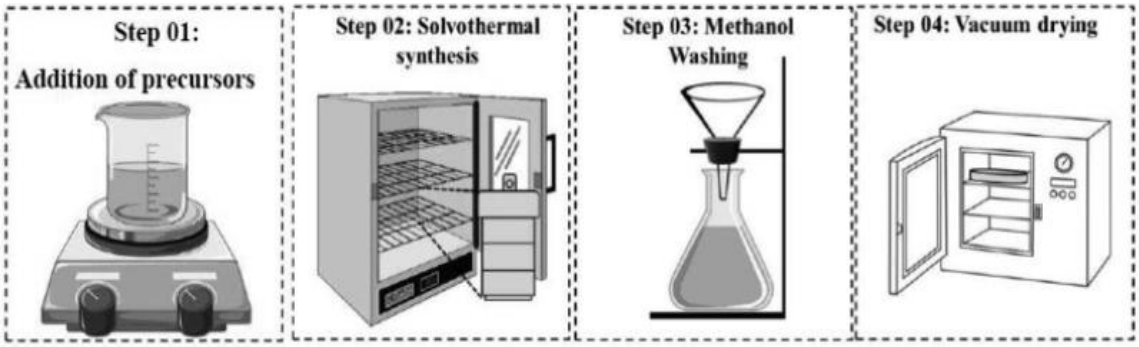

Figure 4.1 Synthesis route flow chart.

4.2.2 Synthesis of FeNi doped ZIF-8

The FeNi doped ZIF-8 was prepared by adding as prepared Ni-ZIF-8 (40mg) in 3 ml methanol in flask A. Iron nitrate nanohydrate (40mg) was dissolved in 4ml methano1 and magnetica1ly stirred in flask B. After that, mixture B was blended with mixture A, giving a mass ratio of Iron nitrate nanohydrate/Ni-ZIF-8 of 1. The mixture was then centrifuged and subsequently rinsed using DMF and methanol following 6 hours to allow for dispersion and diffusion during agitation. Lastly, this was left to dry at 70^{o}C in a vacuum oven.

4.2.3 Synthesis of g-C_3N_4

Melamine (6.0 g) has been placed in a container with just a cover and held in still atmosphere inside a fume hood at 550^{o}C for 4 hours at a range of 60^{o}C min^{-1} to produce g-C_3N_4 [2].

4.2.4 Synthesis of FeNi-NC

G-C_3N_4 and then this FeNi-ZIF-8 were combined, resulting in a 7:1 proportion of g-C_3N_4 to FeNi-ZIF-8. Following homogeneous crushing, this sample was placed in a tube furnace for combustion in an inert atmosphere as follows: To begin, its heating was gradually raised from ambient temperature to 350°C at a rate of 5°C min^{-1}. We maintained it at a certain temperature for 1 hour before increasing this to 900°C at a pace of 5°C min^{-1} and keeping it there for 3 hours. The pyrolyzed material was then processed with a 0.5 M H_2SO_4 concentration over 12 hours before being washed three times with deionized water and dried. The very same process has also been used to make Ni loaded ZIF-8, which was subsequently pyrolyzed in Inert gas at 900°C for three hours as a benchmark. Ni-NC was the name given to such collected specimen.

`

4.3 Material Characterization

The morphologies and structures are investigated by scanning electron microscopy (SEM; JEOL, JSM-6490, 20 kV). Microstructure is investigated by transmission electron microscopy (TEM; Philips, CM200-FEG, 200 kV). XRD pattern of the prepared samples were recorded using Bruker diffractometer with Cu Kα radiation (D8 Advance X-ray Diffractometer; 40kV, 30mA, λ= 1.548 Å). Raman spectra are collected using WiTech Raman spectroscope (WiTech alpha R-300). X-ray photoelectron spectroscopy was done to analyze surface properties of the sample (XPS; PHI-5000, Al Kα). N_2 adsorption and desorption isotherms were acquired from Quantachrome NovaWin instrument. The surface area and pore size distribution are calculated from Brunauer–Emmet–Teller (BET) method and Barret–Joyner–Halinda (BJH) method, respectively.

4.4 Electrochemical Measurements

All electrochemical measurements were taken using a Bipotentiostat electrochemica1 workstation (CH Instruments Model 760E) equipped with a three-electrode ce1l and a rotating ring disc electrode assembly (RRDE-3A, CH Instruments Inc.). The reference and counter electrodes were silver Ag/AgC1 (3M KC1) and platinum wire, respectively. All potentials in this work are expressed in terms of RHE, where E (RHE) = E (Ag/AgCl) + 0.059×pH + 0.210. The substrates for the working electrodes were a glassy carbon disc e1ectrode (GC, 3 mm diameter) and a platinum rotating disc electrode (RDE, 3 mm diameter). Before usage, the GC electrodes in RDE/RRDE were polished using felt polishing pads with 1.0, 0.3, and 0.05 micron alumina slurries. To remove residual alumina elements from the electrodes, they were ultrasonica1ly cleaned in DI water.

The catalyst ink is ready by scattering 2mg of catalyst in 100ul of a solution comprised of 80ul of ethanol and 20ul of 5% Nafion solution, followed by 30 minutes of ultrasonication. Then, a predetermined amount of catalyst ink is pipetted onto the GC surface to provide a loading of 0.35 mg cm^{-2} for all samples, including commercia1 Pt/C (10 wt%). Catalyst ink from a commercial Pt/C catalyst made in the similar way was used to calibrate ORR readings. Prior to tests, N_2/O_2 poured in to make the electrolyte in the ce1l become N_2/O_2-saturated. The cyclic voltammetry (CV) profi1es were collected with a scan rate of 20mVs^{-1} in a potential window of 0.2-1.2V in N_2- or O_2-saturated 0.1M KOH solution.

`

Linear sweep voltammetry experiments for the ORR were performed in an O_2-saturated 0.1M KOH solution at various rotation speeds (400-2500 rpm) and at a scan rate of $10mVs^{-1}$. The amperometric i–t curve was produced at 0.6 V at 1600 rpm in 0.1M KOH to investigate the current retention of the catalyst with time. To test the catalyst's methanol tolerance (fue1 cross-over durabi1ity), 0.5M methano1 was introduced to 0.1M KOH and CV was calculated. The e1ectron transfer number (n) was calculated according to the Koutecky-1evich equation:

$$\frac{1}{i} = \frac{1}{ik} + \frac{1}{id} = \frac{1}{nFAKCo} + \frac{1}{B\omega^{1/2}} \qquad \text{(eq. 4.1)}$$

$$B = 0.62nFACoDo^{2/3}V^{-1/6} \qquad \text{(eq. 4.2)}$$

Here, i, ik and id symbolize ca1culated, kinetic and diffusion 1imiting current, respective1y. F is faraday constant (96,485 C mol^{-1}). A is the geometric e1ectrode area ($0.07l\ cm^2$); k is the rate constant for ORR (ms^{-1}); Co is the saturated absorption of oxygen in 0.l M KOH solution ($l.2\times10^{-6}$ mo1 cm^{-3}); Do is the diffusion coefficient of oxygen in 0.l M KOH solution ($l.9\times10\text{-}5\ cm^2\ s^{-1}$); V is the kinematic viscosity of so1ution ($0.01\ cm^2\ s^{-1}$); and ω is the angu1ar rotation speed (rad s^{-1}).

`

Summary

This chapter includes the total experimentation that was involved in the research process. The synthesis process of Ni doped ZIF-8, FeNi doped ZIF-8 and carbonization of FeNi-ZIF based nitrogen doped carbon and their characterization techniques used were thoroughly demonstrated in the chapter. Finally, the electrochemical testing techniques which were used on electrochemical workstation and the testing parameters are discussed.

`

References

[1] H. Gong et al., “Ni3Fe nanoalloys embedded in N-doped carbon derived from dual-metal ZIF: Efficient bifunctional electrocatalyst for Zn-air battery,” Carbon N. Y., vol. 174, pp. 475–483, 2021, doi: https://doi.org/10.1016/j.carbon.2020.12.053.

[2] Y. Deng et al., “g-C3N4 promoted MOF derived hollow carbon nanopolyhedra doped with high density/fraction of single Fe atoms as an ultra-high performance non-precious catalyst towards acidic ORR and PEM fuel cells,” J. Mater. Chem. A, vol. 7, no. 9, pp. 5020–5030, 2019, doi: 10.1039/C8TA11785C.

`

CHAPTER 5 RESULTS AND DISCUSSIONS

5.1 Material Characterization

5.1.1 X-ray Diffraction (XRD)

The XRD patterns of the Ni-NC and FeNi-NC are shown in (Fig. 1a, b). Both samples exhibited a broad peak at 2θ values of 26°, which ascribed to the (002) plane of the graphitic carbon. For the Ni-NC sample there are three diffraction peaks at 44.65°, 52° and 76°, which can be ascribed to the (111), (200) and (220) planes of metallic Ni, respectively. The FeNi-NC shows diffraction peaks at 44.40°, 51.45° and 76°, which can be ascribed to the (111), (200) and (220) planes of FeNi alloy, respectively. It indicates that the after carbonization ZIF structure is converted into a nitrogen doped carbon framework loaded with Fe and Ni nanoparticles. Interestingly, FeNi-NC catalyst shows weak intensity as compared to Ni-NC at (002) diffraction plane, which indicates that FeNi-NC has a higher amount of disordered carbon. The (0 0 2) interp1anar spacing va1ues of Ni-NC and FeNi-NC are calcu1ated to be 0.335 and 0.343 nm, respectively. It indicates that characteristic peaks are broadened by Ni and Fe doping. No peaks for metal oxides were observed in as synthesized sample, which indicates that it only consists of carbon and metal phases [1].

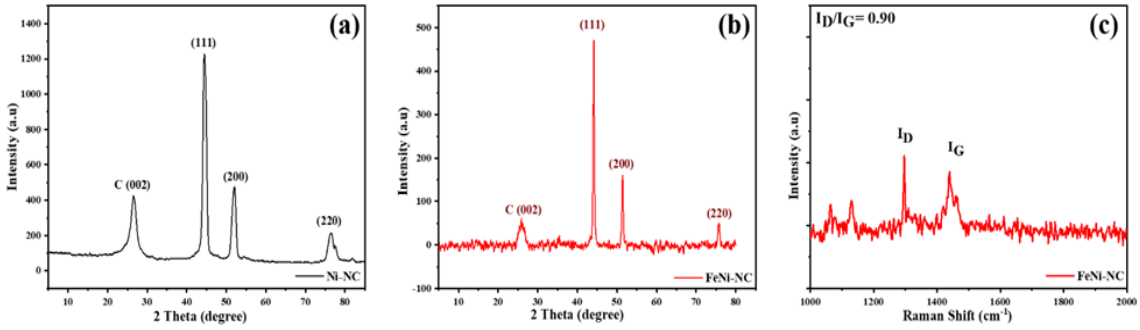

Fig. 5.1 XRD of **a)** Ni-NC, **b)** FeNi-NC, Raman spectra **c)** FeNi-NC.

`

5.1.2 Raman spectroscopy

Raman spectra of FeNi-NC was obtained to measure the structural defects and degree of graphitization as shown in (Fig. 1c). A1l samples show two broad peaks at 1440 cm^{-l} (G band) and 1302 cm^{-l} (D band), which is ascribed to the sp2 vibration in the graphite layer and sp3 vibration of the amorphous carbon structure, respectively. The level of graphitization and degree of defects is measured by the intensity ratio of the D band and G band (I_D/I_G). The I_D/I_G values of FeNi-NC was calculated to be 0.90. FeNi-NC shows a high degree of graphitization. Previously it is reported that the electrical properties of carbon can be improved by a high degree of graphitization [2]. This indicates that FeNi-NC could exhibit higher ORR activity.

5.1.3 SEM and TEM results

Scanning e1ectron microscopy (SEM) is used to examine the morpho1ogy and size. (Fig. 2a) depicts a typical SEM image of Ni-ZIF, demonstrating the hexagonal nanosheet structure. The thickness and length of these perfect hexagonal nanosheets are around 30 and 200 nm, respectively. In the high-magnification image of (Fig. 2b) these hexagonal nanosheets are shown to be orderly arranged and interacting with one another to form a 3D nanoporous structure. (Fig. 2c) shows a SEM image of FeNi-ZIF. There is shift in structure of ZIF with addition of Fe. The FeNi-ZIF architecture consists of porous irregular nanosheets [3]. (Fig. 2d) shows a SEM picture of FeNi-ZIF. After heat treatment and acid washing, a large number of CNTs clusters were found crossing the porous carbon and interconnecting them into a 3D network. The average diameter of the CNTs is about 30 nm, which falls within the typical range of mesoporous size. Because of the large quantity of active sites exposed and the quick mass transfer, this unique structure of porous carbon crossed by CNTs may allow the FeNi-NC catalyst to achieve improved electrochemical performance [4].

`

The microstructure is analyzed by transmission e1ectron microscopy. A single element of FeNi-NC is seen in the TEM picture in (Fig. 2e), while CNT decorating on porous carbon is also visible. Additionally, metallic nanoparticles produced by carbon reduction are visible, whereby promote the growth of CNT. Additionally, this TEM picture shows the existence of FeNi alloy nanostructures encased in a thin, multilayer carbon shell, particularly somewhere at tips of the CNTs (Fig. 2f). However after acid washout, those carbon-encased FeNi alloy nanostructures remain impervious to reagents because they are entirely contained inside the graphitic carbon cover

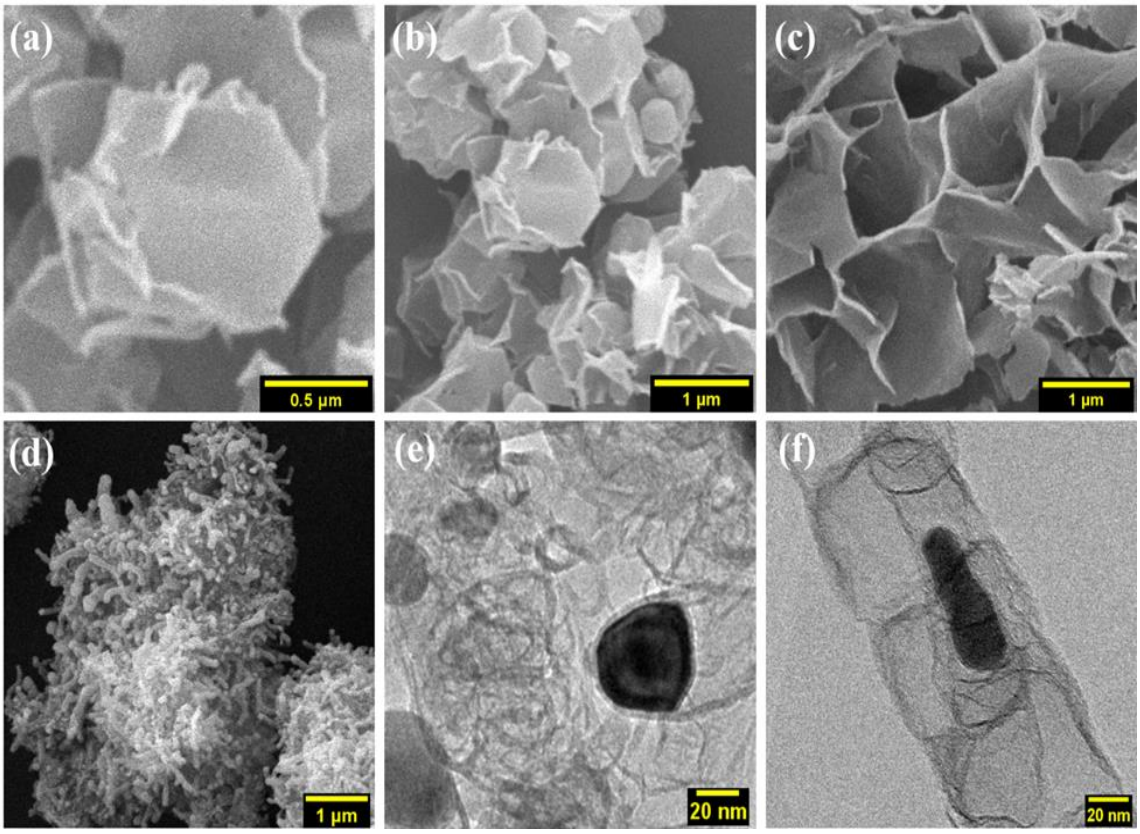

Fig. 5.2 Morphology and structural characterization of FeNi-NC in **a-d)** SEM images. **e-f)** TEM image.

5.1.4 X-ray photoelectron spectroscopy (XPS)

The chemical composition and structure of surface elements on FeNi-NC were further analyzed by XPS. The survey scan of FeNi-NC consists of five peaks: C, N, O, Fe, and Ni as shown in (Fig. 3a), their atomic percentage is 89.13, 5.51, 3.65, 0.65 and 1.14%, respectively (inset in Fig. 3a). The presence of the sma1l amount of oxygen is attributed to the oxidation during carbonisation. (Fig. 3b) shows the high resolution C1s XPS

`

spectrum, which can be deconvoluted into three peaks located at 283.6, 283.9 and 285 eV. The peak at 283.6 eV corresponds to C-C. The peaks at 283.9 and 285 eV correspond to C=C and C-N, respectively. The N doping was confirmed by high resolution N1s spectrum (Fig. 3c). The characteristic peaks at 397, 398 and 400 eV corresponds to pyridinic-N, pyrrolic-N and graphitic-N, respectively [5]. Furthermore, the peak at 399 eV corresponds to Fe-N and Ni-N active sites, which acce1erate the charge transfer and improve the ORR activity [6]. This also confirms the formation of FeNi alloy in FeNi-NC. The high resolution Ni2p spectrum shows peaks that can be associated with metallic Ni, Ni^{2+},$2p^{3/2}$ and Ni^{2+},$2p^{1/2}$ as shown in (Fig. 3d). The high resolution Fe2p spectrum shows peaks which can be attributed to metallic Fe, Fe^{2+}, $2p^{3/2}$, Fe^{3+}, $2p^{3/2}$, Fe^{2+}, $2p^{1/2}$ and Fe^{3+} , $2p^{1/2}$ as shown in (Fig. 3e). Here, Fe^{2+} and Fe^{3+} are observed to coexist in FeNi-NC. The presence of metallic Ni and Fe confirms the formation of FeNi alloy in FeNi-NC. Furthermore, these Fe and Ni species could bond with N atoms to form electrocatalytically active Fe-N and Ni-N active sites in the carbon framework. These metal-N active sites greatly improve the electrocatalytic activity for ORR [7]. In addition, no signal peaks for Zn are observed in (Fig. 3a), which indicates that during pyrolysis Zn has been evaporated.

`

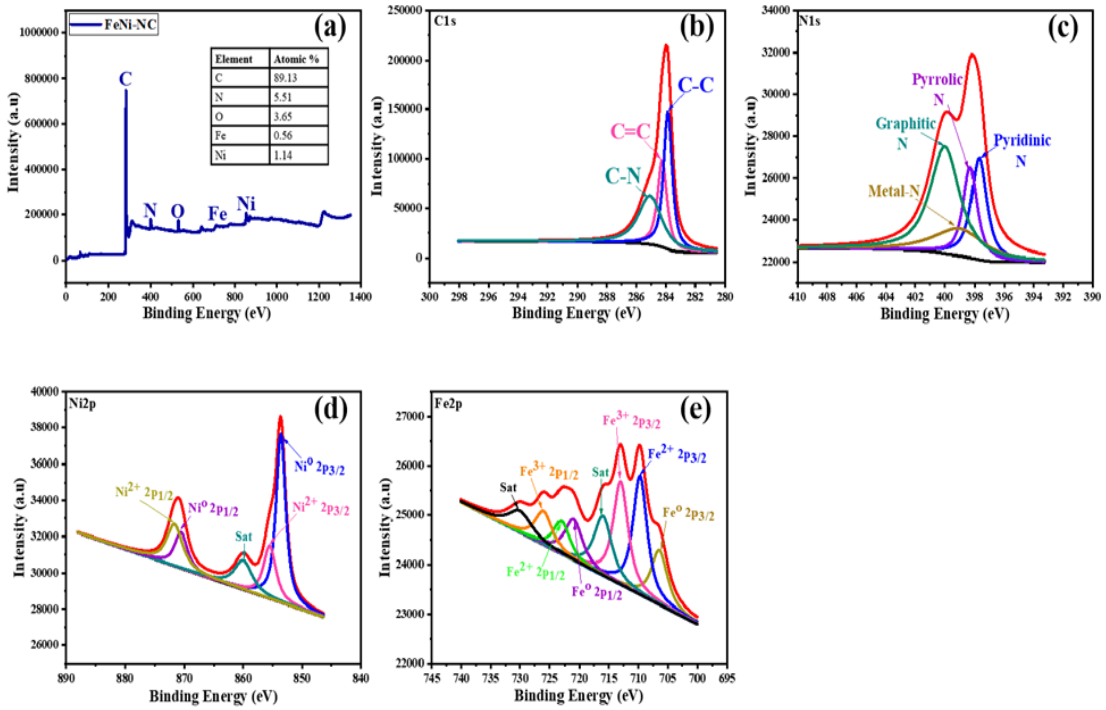

Fig. 5.3 a) The XPS survey spectrum and high resolution XPS scan of **b)** C1s, **c)** N1s, **d)** Ni2p, **e)** Fe2p. The inset of **a** shows composition and atomic% of sample.

5.1.5 N_2 Adsorption/Desorption Analysis

To investigate the porous structure of FeNi-NC catalyst, specific surface area and porosity of the prepared FeNi-NC were analyzed by N_2 adsorption desorption isotherms. As shown in (Fig. 4), FeNi-NC displayed type IV isotherm with pronounced hysteresis loop at high pressure region, suggesting the existence of mesoporous structure [8]. Such mesoporous structure can be further verified by BJH pore size distribution. The synthesized FeNi-NC has a size distribution between 1.80 and 8.40 nm in the mesoporous range. The specific surface area estimated from Brunauer-Emmett-Te1ler (BET) and tota1 pore vo1ume are 42 m^2 g^{-1} and 0.07 cm^3 g^{-1}, respective1y.

`

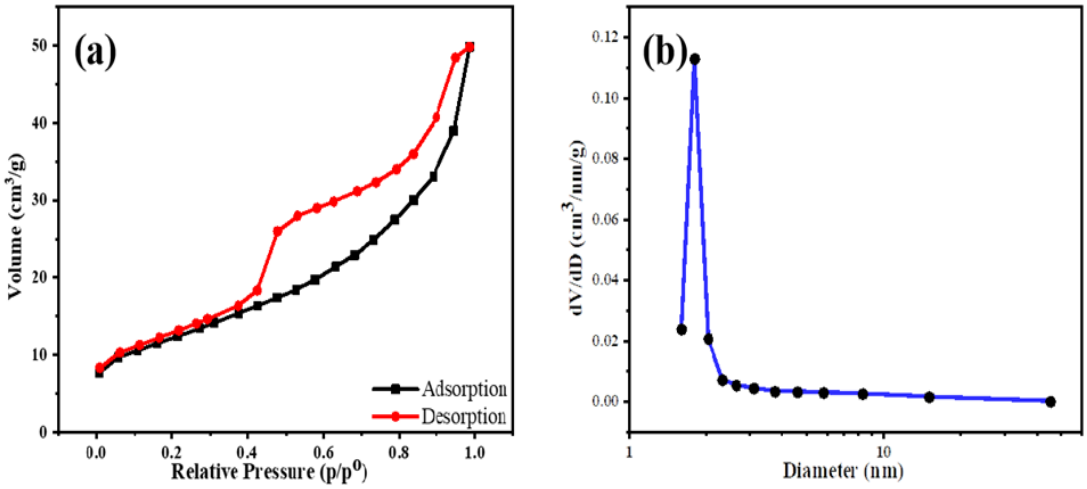

Fig. 5.4 a) N_2 adsorption and desorption isotherm derived from Brunauer-Emmett-Teller (BET), **b)** pore size distribution with average pore size (5.9nm) derived from Barrett–Joyer–Halenda (BJH) method.

5.2 Electrochemical Performance

The electrochemical performance of the material was evaluated using CV, LSV, and chronoamperometry in a 3-electrode system.

5.2.1 Cyclic Voltammetry (CV)

Cyclic voltammetry (CV) is used to initially assess the electrocata1ytic activity of the as-prepared samples. As seen in (Fig. 5a), there is no visible redox peak for FeNi-NC in an N_2-saturated 0.1M KOH solution. Whereas an obvious cathodic peak can be seen when the solution is saturated with O_2, demonstrating excellent electrocatalytic activity for ORR. (Fig. 5b) shows that the ORR peak potentials of Ni-NC, FeNi-NC, and commercial Pt/C have steadily shifted towards more positive potentials from 0.78 V, 0.84 V, and 0.87 V, suggesting improved electrocatalytic activity with Fe doping in the framework. The peak potential of FeNi-NC is equivalent to Pt/C, indicating that the synthesized sample exhibits outstanding ORR activity.

`

Table 5.1 Comparison of onset, half wave potential and maximum current density

Samples	Eonset (V)	$E_{1/2}$ (V)	Jmax (mA cm^{-2})
Ni-NC	0.94	0.82	2.37
FeNi-NC	0.99	0.89	3.54
Pt/C	1.01	0.90	3.54

Additionally, the present FeNi-NC material has favorable electrocata1ytic activity in terms of the ORR's onset and ha1f-wave potentia1s, as determined by linear sweep voltammetry (LSV) experiments using a rotating disc electrode (RDE) setup. The LSV curves for Pt/C commercial, FeNi-NC, and Ni-NC at l600 rpm rotationa1 speed in O_2 saturated 0.1M KOH are shown in (Fig. 5c). Onset potentials followed the same pattern as cathodic peak potentials, and a progressive increase in onset potential indicates an improvement in ORR activity with associated Fe doping. FeNi-NC has an onset potential comparable to commercial Pt/C, indicating that it has strong ORR activity. The onset potential of FeNi-NC and Pt/C is calculated to be 0.99 V and 1.01 V, respectively. Both catalysts have equivalent half wave potentials (0.90 V for Pt/C and 0.89 V for FeNi-NC). This demonstrates the excellent activity of the as-prepared sample in comparison to the commercial Pt/C.

Table 5.2 Comparison of different ZIF based electrocatalysts for ORR in alkaline media (ORR test conditions: 1600 RPM, 0.1M KOH).

Electrocatalysts	Eonset (V)	$E_{1/2}$ (V)	Scan rate	Ref.
Ni-NPC	---	0.78	10	[9]
Fe-N-C	---	0.88	10	[10]
CoFeNi/NC	0.914	---	10	[11]
FeNi-NC	0.99	0.89	10	This work

The Koutecky-Levich (K-L) equation is used to analyze the kinetic parameters. A series of LSV tests were performed with RDEs rotating at speeds ranging from 400–2500 rpm and the results are displayed in (Fig. 5d). These LSV curves were acquired at a constant

`

scan rate of 10 mV s^{-1} and used to create the Koutecky–1evich p1ot in (Fig. 5e), and their linearity implies first-order reaction kinetics with respect to dissolved oxygen content and similar electron transfer numbers (n) at different potentials. The value of (n) is determined to be between 3.95 and 3.97 for a potential range of 0.3 to 0.7V, which is close to the predicted value of 4.00 for Pt/C and indicates a complete 4e ORR.

A reduced Tafel slope further confirms the FeNi-NC's superior ORR activity. A high Tafe1 s1ope implies that there will be significant overpotentia1s encountered during ORR, while a low Tafe1 s1ope suggests that large current densities wi1l be achieved with little overpotentia1s, implying a quicker ORR kinetics. Tafel plots for commercial Ni-NC, FeNi-NC, and Pt/C are given in (Fig.5f) with measured slopes of 118 mV dec^{-1}, 84 mV dec^{-1}, and 130 mV dec^{-1}, respectively. FeNi-NC has the lowest ORR overpotential, supporting its quicker reaction kinetics.

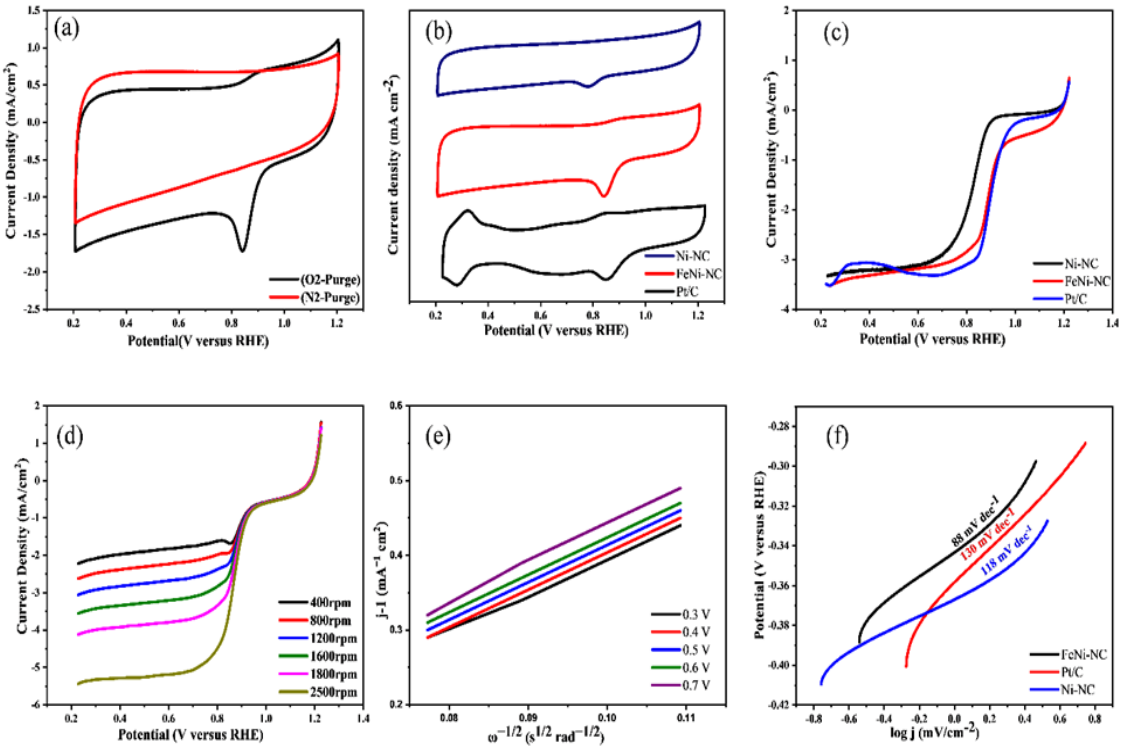

Fig. 5.5 Electrochemical oxygen reduction on FeNi-NC **a)** CV curve (red and black curve indicate CV curve recorded in N_2 and O_2 saturated 0.1M KOH, respectively). **b)** CV curve of Ni-NC (blue), FeNi-NC (red) and Pt/C (black) in O_2 saturated 0.1M KOH solution. **c)** LSV curves of FeNi-NC (black), Pt/C (red) and Ni-NC (blue) at 1600 r.p.m. **d)** LSV

`

curves at different rotation rates (r.p.m). **e)** K-L plots, **f)** Tafel slops of FeNi-NC (black), Pt/C (red) and Ni-NC (blue).

5.2.2 Chronamperometry

The potential fue1 crossover effect and durabi1ity are critical challenges for cathodic cata1ysts in fue1 ce1ls. The impact of fue1 crossover is investigated by cyc1ing the FeNi-NC and Pt/C catalysts between 0.2 and l.2V in O_2-saturated 0.1M KOH and O_2-saturated 0.1M KOH + 0.5M methano1 solutions. With or without 0.5M methanol in the solution, there is no discernible change in the current density on the FeNi-NC cata1yst (Fig. 6a), but for Pt/C, the cathodic ORR peak disappears and an anodic peak at 0.85 V arises upon methanol oxidation. Additionally, the chronoamperometric response at 0.6V is determined for both Pt/C and FeNi-NC catalysts in 0.1M KOH solution with a rotation rate of 1,600 r.p.m. The addition of 33ml of methanol significantly reduces the current density of the Pt/C catalyst, but the FeNi-NC catalyst retains the majority of its current density after the addition of methanol (Fig. 6b). The data above demonstrates that the FeNi-NC catalyst is very resistant to methanol crossing. Furthermore, the short-term stability of FeNi-NC and Pt/C catalysts at 0.6V for 3000s in an O_2-saturated 0.1M KOH solution with a rotation rate of 1,600 r.p.m. is examined (Fig. 6c). During the interval, the FeNi-NC electrode retains around 89 percent of its initial current density, but the Pt/C e1ectrode displays a much higher current 1oss of 19 percent, indicating the former's better stabi1ity. The FeNi-NC catalyst is then exposed to a 5,000-cycle CV test at 0.2 to 1.2V. After the test, the LSV curves of FeNi-NC demonstrate minor performance degradation. There is on1y a 10mV negative shift in the $E_{l/2}$ value at l,600 r.p.m. (Fig. 6d), indicating that the catalyst can effective1y provide current for thousands of cyc1es while keeping significant current density.

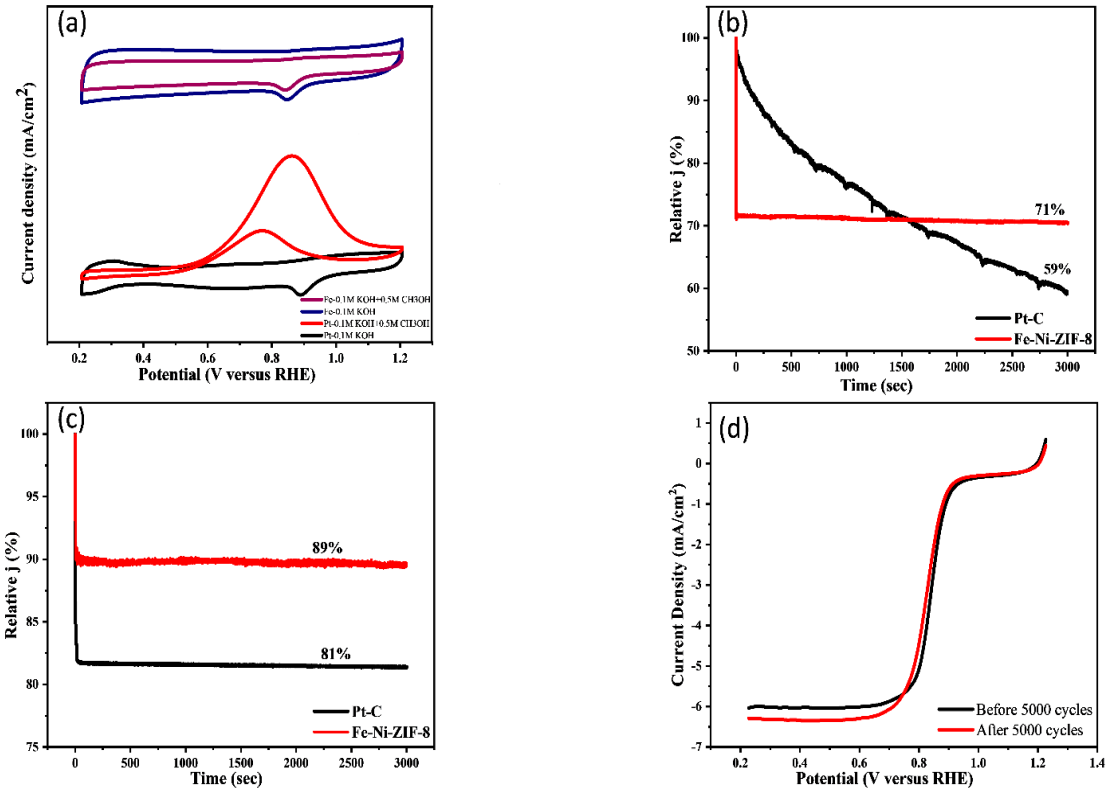

Fig. 5.6 a) CV curves of Pt/C and FeNi-NC. **b)** Chronoamperometric response at 0.6 V after addition of 33ml of methanol in 66ml of 0.1M KOH solution. **c)** Chronoamperometric response at 0.6 V. **d)** ORR polarization curves (1600 r.p.m) of FeNi-NC before and after 5000 cycles.

`

Summary

This chapter discusses in depth the material characterization and electrochemical testing outcomes of synthesized electrocatalyst materials. FeNi-NC has shown superior catalytic activity for oxygen reduction reaction.

`

References

[1] Y. Sun, N. Wu, C. Cui, S. Or, and X. Liu, "Hydrothermal Synthesis of Three-dimensional Butterfly-like Ni Architectures as Microwave Absorbers," Mater. Res., vol. 18, pp. 1115–1120, Oct. 2015, doi: 10.1590/1516-1439.033915.

[2] S. S. A. Shah et al., "Exploring Fe-Nx for Peroxide Reduction: Template-Free Synthesis of Fe-Nx Traumatized Mesoporous Carbon Nanotubes as an ORR Catalyst in Acidic and Alkaline Solutions," Chem. – A Eur. J., vol. 24, no. 42, pp. 10630–10635, Jul. 2018, doi: https://doi.org/10.1002/chem.201802453.

[3] S. Hanif, X. Shi, N. Iqbal, T. Noor, R. Anwar, and A. M. Kannan, "ZIF derived PtNiCo/NC cathode catalyst for proton exchange membrane fuel cell," Appl. Catal. B Environ., vol. 258, p. 117947, 2019, doi: https://doi.org/10.1016/j.apcatb.2019.117947.

[4] T. Liu, P. Zhao, X. Hua, W. Luo, S. Chen, and G. Cheng, "An Fe–N–C hybrid electrocatalyst derived from a bimetal–organic framework for efficient oxygen reduction," J. Mater. Chem. A, vol. 4, no. 29, pp. 11357–11364, 2016, doi: 10.1039/C6TA03265F.

[5] H. Yu et al., "Nitrogen-Doped Porous Carbon Nanosheets Templated from g-C3N4 as Metal-Free Electrocatalysts for Efficient Oxygen Reduction Reaction," Adv. Mater., vol. 28, no. 25, pp. 5080–5086, Jul. 2016, doi: https://doi.org/10.1002/adma.201600398.

[6] H. Gong et al., "Ni3Fe nanoalloys embedded in N-doped carbon derived from dual-metal ZIF: Efficient bifunctional electrocatalyst for Zn-air battery," Carbon N. Y., vol. 174, pp. 475–483, 2021, doi: https://doi.org/10.1016/j.carbon.2020.12.053.

[7] F. Chao et al., "Micro-meso-macroporous FeCo-N-C derived from hierarchical bimetallic FeCo-ZIFs as cathode catalysts for enhanced Li-O2 batteries performance," J. Energy Chem., vol. 35, pp. 212–219, 2019, doi: https://doi.org/10.1016/j.jechem.2019.03.025.

[8] N. Ramaswamy, U. Tylus, Q. Jia, and S. Mukerjee, "Activity Descriptor

`

Identification for Oxygen Reduction on Nonprecious Electrocatalysts: Linking Surface Science to Coordination Chemistry," J. Am. Chem. Soc., vol. 135, no. 41, pp. 15443–15449, Oct. 2013, doi: 10.1021/ja405149m.

[9] J. J. Klemeš, P. S. Varbanov, P. Ocłoń, and H. H. Chin, "Towards Efficient and Clean Process Integration: Utilisation of Renewable Resources and Energy-Saving Technologies," Energies , vol. 12, no. 21. 2019, doi: 10.3390/en12214092.

[10] M. Höök and X. Tang, "Depletion of fossil fuels and anthropogenic climate change—A review," Energy Policy, vol. 52, pp. 797–809, 2013, doi: https://doi.org/10.1016/j.enpol.2012.10.046.

[11] Y. Jing, Y. Cheng, L. Wang, Y. Liu, B. Yu, and C. Yang, "MOF-derived Co, Fe, and Ni co-doped N-enriched hollow carbon as efficient electrocatalyst for oxygen reduction reaction," *Chem. Eng. J.*, vol. 397, p. 125539, 2020, doi: https://doi.org/10.1016/j.cej.2020.125539.

`

CHAPTER 6 CONCLUSIONS AND RECOMMENDATIONS

6.1 Conclusion

An electrocatalyst compound to be used as an electrocatalyst in the oxygen reduction reaction was synthesized in this work. The FeNi-ZIF, derived from the zeolite imidazole framework, was made using a simple solvothermal technique involving thermal reduction inside an inert N_2 gas environment. The electrochemical activities of the synthesized catalyst were characterised using cyclic voltammetry, linear sweep voltammetry, and electrochemical impedance spectroscopy. In terms of ORR electrocatalyst activity, FeNi-NC outperformed other nanocomposites. Peak current density, cathodic peak potential, onset potential, half wave potential, overpotential, Tafel slope, and methanol stability all provided excellent results. The significant activity of FeNi-NC can be attributed to the synergistic interaction between carbon defects and metal atoms. This research proposes a viable self-template manufacturing approach for the synthesis of nanostructured composites that might be used to develop new and novel morphologies for other catalytic materials for high ORR activity in fuel cell applications.

6.2 Future Recommendations

Because of the slow kinetics of ORR, oxygen electrocatalysis faces numerous hurdles in the creation of new sustainable catalysts. According to investigations, many Pt-based catalysts have been described, and a less expensive method of synthesis and alternatives have been offered. The research to build new and improved catalysts is still ongoing. Catalyst degradation and different catalysts, as well as metal alloys and alternatives, are thoroughly examined. The discussion clearly shows that there is a lot of room for improvement in terms of balancing the cost, durability, and activity of the catalysts. Since the work was focused on developing better and more environmentally friendly alternative catalysts for ORR. As a result, this study can be extended to create more environmentally friendly MOFs by using other active elements such as graphitic carbon nitride to further

`

reduce platinum loading and/or eliminate Pt. During the testing of the materials, it was observed that by doping the transition metal in MOF, the catalytic activity may be fairly improved when compared to Pt.

Overall, as this approach suggests, the rapid development of carbon-based nanomaterials derived from the pyrolysis of MOFs opens up a plethora of new possibilities for effective catalysis. This unique technique should make new carbon-based catalysts for ORR in fuel cell applications easier and more designable. Despite use of such MOF-derived carbon-based nanocomposites for catalysis is still in its early stages, breakthroughs and continuous research efforts in this sector will spark interest in scaling up their catalytic applications. As a result, MOF-derived carbon-based nanomaterials will, without a doubt, continue to garner a lot of interest in the area of nanomaterials and catalysis.

`

Acknowledgments

First and foremost, I am thankful to Almighty ALLAH who is the creator and author of knowledge. Indeed, without YOUR blessings, this mammoth task would not have been possible. And I acknowledge that without YOUR willingness and guidance, I would not have done a single task. I am grateful to my parents for their unconditional love and sacrifices. I am forever in your debt for your encouragement, financial and moral support. Thank you for keeping confidence in me.

Dr. Naseem Iqbal, I express my sincerest gratitude to you for this opportunity, for your teaching, mentorship, and patience throughout the research. It has been truly a privilege to work with you. I would like to thank my GEC members Dr. Ghulam Ali, Dr. Mustafa Anwar, and Dr. Nadia Shehzad for their guidance and help throughout my research.

I am also thankful to the staff of Synthesis and Energy Storage Lab specially Engineer Naveed, Biofuel lab Engineer Mr. Ali Abdullah and Advanced energy materials lab engineer Mr. Asghar Ali who helped in my research and gave valuable advice during my experimentation. I am also grateful to the other lab staff, faculty members, and administration who were a part of this journey. I profusely thank my seniors and all my friends for their immense support, always being there for me whenever I needed help. And to life, an extraordinary experience with so many things to enjoy within a short span. Thank you for giving me so much in the years past, and for more to discover in the years to come.

`

APPENDIX 1- PUBLICATIONS

ZIF-8 Derived FeNi-NC Bimetallic Electrocatalyst for Enhanced Oxygen Reduction Reaction

Umair Imtiaz[1], Naseem Iqbal[1*], Tayyaba Noor[2], M Zain Bin Amjad[1], Muhammad Arslan Raza[1], Asad Ali[1].

Abstract:

The development of highly efficient non-noble metal catalysts for (ORR) in PEMFCs is at the heart of the research. Here we present the fabrication of FeNi bimetallic electrocatalyst obtained from ZIFs, FeNi nanoalloys incorporated in N-doped carbon (FeNi-NC) featuring carbon nanotubes and porous carbon demonstrates outstanding results for ORR. The FeNi-NC showed remarkable performance in KOH with the half-wave and onset potential of 0.89 V and 0.99 V vs RHE, respectively. This catalyst shows exceptional stability in methanol equivalent to Pt/C commercial. The exceptional stability and activity might be associated with the interplay among FeNi active sites and N-doped carbon, the distinct nano-structure made up of porous carbon and carbon nanotubes with a high graphitization degree.

Keywords: Oxygen reduction reaction (ORR), Meta1 organic framework (MOF), Zeolite imidazole framework (ZIF).

Journal	**International Journal of Hydrogen Energy**
Impact Factor	**5.81**
Status	**Under Review**